

1 **Observation and modelling of atmospheric OH and HO₂**
2 **radicals at a subtropical rural site and implications for**
3 **secondary pollutants**

4 Zhouxing Zou^{1#}, Tianshu Chen^{1#}, Qianjie Chen¹, Weihang Sun¹, Shichun Han¹,
5 Zhuoyue Ren², Xinyi Li², Wei Song², Aoqi Ge², Qi Wang², Xiao Tian², Chenglei Pei³,
6 Xinming Wang², Yanli Zhang², and Tao Wang¹

7 [#]These authors contributed equally to this work

8 ¹ Department of Civil and Environmental Engineering, The Hong Kong Polytechnic
9 University, Hong Kong, China

10 ² Guangzhou Institute of Geochemistry, Chinese Academy of Sciences, Guangzhou,
11 China

12 ³Guangdong Province Guangzhou Ecological Environment Monitoring Center Station,
13 Guangzhou 510030, China.

14 Correspondence to: Tao Wang (tao.wang@polyu.edu.hk)

15 **Abstract**

16 HO_x radicals (OH and HO₂) are crucial oxidants that determine atmospheric oxidation
17 capacity and the production of secondary pollutants; however, their sources and sinks
18 remain incompletely understood in certain rural, forest and maritime environments.
19 This study measured HO₂ and OH concentrations using a chemical ionisation mass
20 spectrometer at a subtropical rural site in southern China from 12 November to 19
21 December 2022. The average peak concentrations were $3.50 \pm 2.47 \times 10^6 \text{ cm}^{-3}$ for OH
22 and $1.34 \pm 0.93 \times 10^8 \text{ cm}^{-3}$ for HO₂. Calculations based on an observation-constrained
23 chemical model revealed an overestimation of HO₂ and OH concentrations during
24 warm periods of the field study. Sensitivity tests suggest that adding HO_x sinks or a
25 HO₂ recycle process to the model could improve the model performance. The over-
26 simulation of HO_x in the model resulted in overestimations of production rates of ozone
27 by up to 98% for ozone and up to 341% for nitric acid. Our study highlights the need
28 for further improving understanding of the sources/sinks of OH and HO₂ and
29 representation of them in air quality models.

1 **1. Introduction**

2 The HO_x family, comprising hydroxyl (OH) and peroxy radicals (HO₂), plays a
3 pivotal role in the Earth's atmosphere by driving photochemical processes that influence
4 the air composition and chemistry. OH radicals are primarily produced by the
5 photolysis of ozone (O₃), nitrous acid (HONO), and ozonolysis of alkenes. They initiate
6 the oxidation of CO and most volatile organic compounds (VOCs), producing HO₂ and
7 other peroxy radicals (RO₂, where R represents an alkyl group). HO₂ is also generated
8 from the photolysis of oxygenated VOCs (OVOCs) and by reactions between OVOCs
9 and OH. In the presence of NO, RO₂ radicals are converted to HO₂ and then to OH
10 radicals buffering OH concentrations and maintaining atmospheric oxidation capacity.
11 (Stone et al., 2012). These interactions are crucial in the formation of photochemical
12 smog and secondary organic aerosol (SOA), which generate NO₂, O₃ and highly
13 oxygenated molecules. HO_x radicals are removed through reactions of OH with
14 inorganic trace gases, self-reactions among radicals, peroxyacetyl nitrate (PAN)
15 formation, and the heterogeneous uptake by aerosols, subsequently contributing to
16 atmospheric acidification and aerosol formation by the production of H₂SO₄ and HNO₃.

17 See Figure S1 and Table S1 for detailed processes and chemical reactions.

18 The accuracy of model-predicted OH is a crucial indicator for assessing our
19 understanding of the atmosphere processes (Heard and Pilling, 2003). There is a
20 longstanding debate regarding the discrepancies between simulated and observed
21 radical concentrations under low NO_x condition which remains a significant issue
22 (Hofzumahaus et al., 2009; Stone et al., 2012; Zou et al., 2023). Previous studies have
23 shown that models generally predict OH levels well in polluted conditions (NO > 1
24 ppb), but notable overestimation were observed under low NO and aged conditions,
25 such as coastal areas (Kanaya et al., 2007; Zou et al., 2023), marine boundary layers
26 (Berresheim et al., 2002; Carslaw et al., 1999), and the rural area (Bottorff et al., 2023;
27 Kanaya et al., 2012). Missing OH sinks from both measurement or chemical mechanism
28 were proposed as the primary reason for the overestimation (Lou et al., 2010; Yang et
29 al., 2016; Hansen et al., 2014 Thames et al., 2020). Underestimation of OH

1 concentrations were also observed in high biogenic VOCs (BVOCs) and low NO (<1
2 ppb) conditions which generally happen in the subtropical or tropical area
3 (Hofzumahaus et al., 2009; Lelieveld et al., 2008; Tan et al., 2001; Whalley et al., 2011).
4 After considering a new OH regeneration mechanism (Wennberg et al., 2018; Novelli
5 et al., 2020) and a measurement interference (Feiner et al., 2016; Hens et al., 2014; Mao
6 et al., 2012; Novelli et al., 2014; Woodward-Massey et al., 2020), daytime OH
7 concentration could be reasonably reproduced by the model in the high BVOC
8 conditions, with some unresolved underestimation in the evening (Jeong et al., 2022;
9 Lew et al., 2020; Tan et al., 2019). Those results called for more measurement and
10 modelling in the subtropical and tropical rural areas.

11 HO₂ concentrations were consistently underpredicted in the polluted urban sites
12 (Ma et al., 2019; Yang et al., 2021; Ma et al., 2022), with no clear trends in relatively
13 clean regions. Some studies reported good agreement between measurement and model
14 prediction (Feiner et al., 2016; Lew et al., 2020), whereas others indicated model
15 overprediction (Bottorff et al., 2023; Griffith et al., 2013) and underprediction (Kim et
16 al., 2013; Mallik et al., 2018 Tan et al., 2017; Whalley et al., 2010). These discrepancies
17 may be attributed to several factors, including: measurement interference caused by
18 RO₂ recycling in environments rich in BVOCs or aromatics (Fuchs et al., 2011),
19 uncertainties associated with heterogeneous uptake in box models (Yang et al., 2022),
20 and the outflow (or entrainment) of reservoir species like PAN (Griffith et al., 2013)
21 (Whalley et al., 2010) . Despite these advances, it remains difficult to pin down the
22 exact causes of the model-measurement discrepancies in some of the previous studies.

23 In the present study, we measured concentrations of OH and HO₂ using a
24 quadrupole chemical ionization mass spectrometer (PolyU-CIMS) from November to
25 December 2022 at a subtropical rural site of southern China. We test model's capability
26 in reproducing the radical concentrations and elucidate factors contributing to
27 discrepancy under varying temperature, VOCs, and NO_x conditions. The Methodology
28 section describes the measurement site, the principle and the configuration of PolyU-
29 CIMS, and the setup of chemical box model. The Results and Discussion section details

1 our findings, providing a comprehensive analysis of the radical concentrations and
2 exploring the discrepancies between observed data and model predictions. By
3 employing an observation-constrained box model, we analyzed the radical budgets and
4 investigated potential causes for these discrepancies. The study concludes with a
5 discussion of the implications of these findings.

6 **2. Methodology**

7 **2.1 Measurement Site**

8 The field campaign was conducted at the Conghua Liangkou Air Monitoring
9 Station (23°44'47"N, 113°47'06"E, 200m, above sea level) from November 12 to
10 December 19, 2022 (Figure 1). The site is located at the northern part of the Pearl River
11 Delta (PRD), approximately 80 kilometers from the densely populated areas of the PRD
12 and nestled within the Liuxi River National Forest Park (an evergreen broad-leaf forest).
13 The site is situated just north of the G105 national highway and around 0.5 kilometer
14 east from Liangkou town. Even though it is close to the road, the traffic was generally
15 limited during the observation period due to the coronavirus disease pandemic (COVID
16 19). The site is subjected to the BVOCs emission, predominantly isoprene, from the
17 surrounding forest when the daytime temperature is exceeding 20°C, and NO emissions
18 from the nearby national highway, particularly during periods of low wind speeds. The
19 measurements comprised trace gases including O₃, NO, NO₂, CO, HONO, VOCs,
20 OVOCs, meteorological data such as relative humidity (RH), temperature, and
21 photolysis frequencies of HONO, NO₂, O₃, H₂O₂, and HCHO. Details about the
22 instruments are shown in Table S2.



Figure 1 Geographic location of measurement site (Liangkou Air Monitoring station 23°44'47"N, 113°47'06"E, 200 m a.s.l. labelled by the red inverted triangle) in Conghua, Guangdong Province, South China. The map is sourced from © Google Earth and © Amap.

2.2 Radical measurement principle

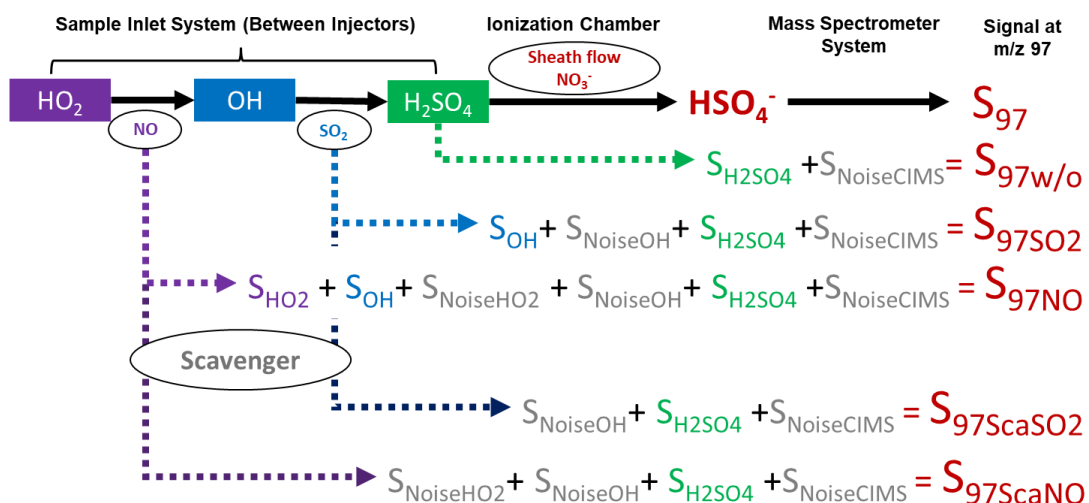
OH and HO₂ radicals were measured using the Hong Kong Polytechnic University quadrupole Chemical Ionization Mass Spectrometer (PolyU-CIMS), which was used in a previous study for OH measurement (Zou et al., 2023). The use of CIMS for OH measurement was pioneered by Eisele and Tanner, (1991), with subsequent enhancements in measurement accuracy (Eisele and Tanner, 1993; Tanner et al., 1997; Tanner and Eisele, 1995) and adoption of inlets for simultaneous measurements of HO₂ and RO₂ (Edwards et al., 2003; Sjostedt et al., 2007), H₂SO₄ (Mauldin III et al., 2004), and OH reactivity (Muller et al., 2018).

Figure 2 illustrates the measurement principle of the PolyU-CIMS used in this campaign. Briefly, the ambient OH radicals are converted to H₂SO₄ in the sample inlet system by reacting with SO₂ (R21 in the reaction Table S1) which is then transformed to HSO₄⁻ ion clusters in the ionization chamber by the reactions with a reagent gas in

1 sheath flow (HNO_3 , R24 to 27), and ultimately dissociated (R29) for detection by the
 2 mass spectrometer system at m/z 97 (S_{97SO_2} in Figure 2). To mitigate interference and
 3 noise, scavenger gases (C_3F_6 in this study) were introduced to scavenge the ambient
 4 OH, creating a background signal (R23, $\text{S}_{97\text{ScasO}_2}$ in Figure 2). See details about the
 5 scavenge efficiency in Text S3 in SI. The ambient OH radicals signal (S_{OH}) is then
 6 determined by the subtracting $\text{S}_{97\text{ScasO}_2}$ from S_{97SO_2} . The OH concentration is calculated
 7 using the following equation:

$$8 \quad [\text{OH}] = \frac{1}{C_{\text{OH}}} \times \frac{\text{S}_{\text{OH}}}{\text{S}_{62}} \quad (\text{E1})$$

9 Where C_{OH} represents the calibration factors of OH, and S_{62} is the signal corresponding
 10 to the reagent ion (NO_3^-). The detailed calibration procedure for OH is outlined in
 11 previous studies (Kürten et al., 2012; Zou et al., 2023) and also in Test S1.



12 **Figure 2** Flow chart depicting the relationship between measurement species and signal intensity at
 13 m/z 97 (S_{97}) with various gas injections. The color-filled grids labeled the ambient species, while
 14 oval shape labeled the species injected into the sample flow. Signal intensities with different gas
 15 additions to the sample flow are represented by $\text{S}_{97\text{w/o}}$, S_{97SO_2} , $\text{S}_{97\text{NO}}$, $\text{S}_{97\text{ScasO}_2}$, and $\text{S}_{97\text{ScasNO}}$. The
 16 signals corresponding to ambient OH, HO_2 , H_2SO_4 and noise from OH measurement, HO_2
 17 measurement and the CIMS denoted as S_{OH} , S_{HO_2} , $\text{S}_{\text{H}_2\text{SO}_4}$, $\text{S}_{\text{NoiseOH}}$, $\text{S}_{\text{NoiseHO}_2}$ and $\text{S}_{\text{NoiseCIMS}}$,
 18 respectively.

20 To measure ambient HO_2 , NO is injected into the sample flow, converting HO_2 to
 21 OH (R11). This converted OH then follows the same reaction pathway (R21, R24 to
 22 R27, and R29) and is measured at m/z 97 ($\text{S}_{97\text{NO}}$ in Figure 2). Similar to the OH
 23 measurement, the background signal for HO_2 ($\text{S}_{97\text{ScasNO}}$ in Figure 2) is determined by

1 introducing the scavenger gas. The corresponding signal for ambient HO₂ (S_{HO2} in
2 Figure 2) is determined by subtracting S_{97ScNO} and S_{OH} from S_{97NO}. The HO₂
3 concentration is calculated using a similar equation to E1, by replacing S_{OH}, and C_{OH} to
4 S_{HO2} and C_{HO2}, respectively (E2).

5

$$[HO_2] = \frac{1}{c_{HO_2}} \times \frac{S_{HO_2}}{S_{62}} \quad (E2)$$

6 The procedure for determination of HO₂ calibration factor, C_{HO2}, is akin to that for C_{OH}
7 (Text S1). The calibration tube generates equal amounts of radicals (R30 in SI,
8 [OH]/[HO₂] = 1), allowing for simultaneous calibration of HO₂ and OH with and
9 without NO addition to the sample flow.

10 Interference from RO₂ can affect HO₂ measurements, potentially resulting in an
11 overestimation of ambient HO₂ levels (Edwards et al., 2003; Fuchs et al., 2014; Hanke
12 et al., 2002). In our study, both the experimental and modelling results did not show
13 significant interference under our environmental conditions (Text S4.3).

14 Compared to its configuration in the previous campaign (Zou et al., 2023), the
15 PolyU-CIMS has been upgraded for simultaneous HO₂ measurements. See Figure S2,
16 Text S2 on modification for HO₂ measurement; and Text S5 for measurement duty
17 cycle. Apart from the modifications, the PolyU-CIMS's setting, and configurations
18 remained the same as those in the previous campaign (Table S3). With the updated
19 configuration, the PolyU-CIMS achieved the simultaneous measurement for the three
20 gases.

21 The calibration factor, detection limit and accuracy were $1.09 \times 10^{-8} \text{ cm}^{-3}$, 3×10^5
22 cm^{-3} , and 44% for OH; $6.01 \times 10^{-9} \text{ cm}^{-3}$, $2 \times 10^6 \text{ cm}^{-3}$, and 46% for HO₂; and $1.09 \times 10^{-8} \text{ cm}^{-3}$, $1 \times 10^5 \text{ cm}^{-3}$, and 40% for H₂SO₄, respectively (Table S3).

24 **2.3 Box Model**

25 HO_x concentrations in this study were simulated using the Framework for 0-D
26 Atmospheric Modelling (F0AM, Wolfe et al., 2016) with the Master Chemical
27 Mechanism (MCM) v3.3.1 (<http://mcm.leeds.ac.uk/MCM>), which encompasses over
28 6700 species and 17000 reactions. MCM v3.3.1 features a near-explicit chemical
29 mechanism, including isoprene degradation and OH regeneration mechanisms. This

1 mechanism has been previously employed for investigating HO_x chemistry and
2 conducting budget analyses (Slater et al., 2020; Tan et al., 2018; Zou et al., 2023). The
3 gas-phase chlorine chemistry described by Xu et al., (2015) and Wang et al. (2019)
4 were included in the model (Chen et al., 2022).

5 In the baseline scenario, the observation data were aggregated into one-hour
6 intervals to provide input for the model, initially constraining it without incorporating
7 observed OH and HO₂ data. For the assessment of ozone formation rates, the model
8 was adjusted to include constraints based on the actual measured concentrations of OH
9 and HO₂. Observed VOCs were categorized into anthropogenic origin (AVOCs),
10 including species from petroleum gas and industrial solvent evaporation (alkenes,
11 alkenes, benzene, and TEXs - toluene, ethylbenzene, and xylenes), and OVOCs
12 comprising aldehydes, ketones, and acids. The sole BVOCs measured in this study was
13 isoprene. Methacrolein (MACR), a derivative of isoprene, is distinctively classified
14 among the biogenically sourced OVOCs for further discussion. Physical processes like
15 deposition and entrainment in the model were represented by a first-order physical loss
16 with a 24-hour lifetime for all species (Chen et al., 2022; Wolfe et al., 2016; Zou et al.,
17 2023). The model also included the heterogeneous uptake of HO₂ by aerosols,
18 represented as a pseudo-first order loss (Jacob, 2000):

$$19 \frac{d[HO_2]}{dt} = -k_{HO_2}[HO_2] \quad (E3)$$

$$20 k_{HO_2} = \frac{V_{HO_2} \times S_a \times \gamma_{HO_2}}{4} \quad (E4)$$

$$21 v_{HO_2} = \sqrt{\frac{8RT}{\pi \times M_{HO_2}}} \quad (E5)$$

22 Here, k_{HO_2} represents the first-order loss rate coefficient of HO₂ by aerosol uptake,
23 determined by the effective HO₂ uptake coefficient γ_{HO_2} (0.1, Guo et al., 2019), the
24 mean molecular velocity of HO₂ (v_{HO_2}), the aerosol surface area concentration (S_a)
25 measured by the Scanning Mobility Particle Sizing (SMPS); and the molecular mass of
26 HO₂ ($M_{HO_2} = 17$ g/mol). As aerosol and aqueous phase chemistry were not included in
27 the model, it was assumed that the heterogeneous HO₂ loss would not lead to further
28 reactions (Guo et al., 2019). For each day, a three-day spin-up was performed with

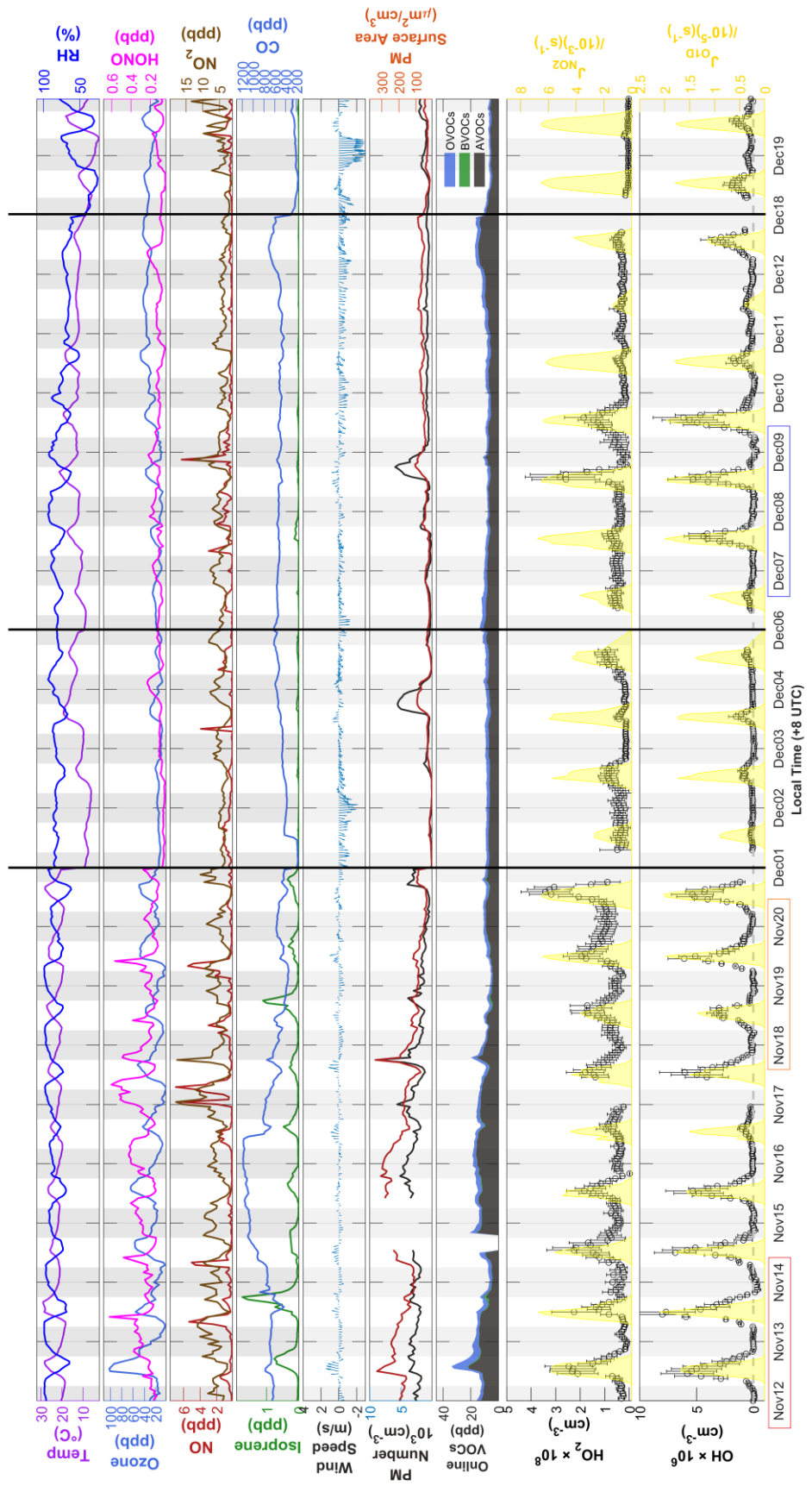
1 constant inputs to establish stable model chemistry and reduce the uncertainty of
2 unconstrained species. See Text S6 for model set up for interferences assessment.

3 **3. Results and Discussion**

4 **3.1 Results from Observations**

5 **3.1.1 Overview**

6 Figure 3 illustrates a time series showing observed concentrations of radical and
7 trace gases, along with meteorological parameters, from 12 November to 19 December
8 2022. In November, the conditions were characterised by warm temperatures ranging
9 from 29°C to 19°C and high relative humidity averaging 86%. In contrast, December
10 witnessed a significant decrease in temperature (ranging from 20°C to 9°C) and a
11 reduction in relative humidity (averaging 72%). Wind speeds during the campaign were
12 generally low, averaging 0.9 ± 0.6 m/s and typically remaining below 3.0 m/s, with
13 higher speeds occurring towards the end of December. In November, daytime winds
14 predominantly blew from the south, while nighttime winds came from the north. In
15 December, northerly winds predominated both day and night. Detailed hourly wind
16 speed and direction data are illustrated in Figure 3, and wind roses are shown in Figure
17 S3. On days with low wind speeds (< 0.5 m/s), NOx emissions from the G105 national
18 highway significantly influenced chemical measurements at the monitoring site,
19 causing morning NO levels to peak at several parts per billion (ppb). Isoprene
20 concentrations peaked in the afternoons, ranging from 0.2 to 1.7 ppb in November and
21 dropping to < 0.1 ppb in December. Other trace gases and particulate matter levels were
22 higher in November than in December.



1 **Figure 3** Time series of HO₂ and OH radicals between 12 November and 19 December, including
2 measured weather conditions (temperature, RH, wind speed, and wind direction), primary sources
3 of HO_x radicals (ozone, HONO), important sinks of the radicals (CO, isoprene, and VOCs), and
4 photolysis frequencies of NO₂ (J_{NO2}) and ozone (J_{O3D}). Non-continuous days during the campaign
5 are delineated by a black line. The PRD, CEC, and CNC periods for further analysis were labelled
6 in red, orange, and blue. The x-axis is in local time (+8 UTC).

7 Throughout the campaign, the daytime concentrations of OH and HO₂ consistently
8 exceeded detection limits and showed distinct diurnal patterns. The OH concentrations
9 typically peaked around midday, while the HO₂ levels reached their maximum
10 approximately one to two hours later (Figure S4). The daily maximum concentration of
11 OH varied significantly, ranging from $8.00 \times 10^6 \text{ cm}^{-3}$ to nearly the detection limit of
12 $2.54 \times 10^5 \text{ cm}^{-3}$, with an average of $3.50 \pm 2.47 \times 10^6 \text{ cm}^{-3}$ (Table 1). Similarly, the
13 daily maximum concentration of HO₂ varied from $3.42 \times 10^8 \text{ cm}^{-3}$ to $2.17 \times 10^7 \text{ cm}^{-3}$,
14 averaging $1.34 \pm 0.93 \times 10^8 \text{ cm}^{-3}$ (Table 1). At nighttime, while the HO₂ levels
15 generally remained above the detection threshold, the OH concentrations frequently
16 approached the threshold. The average nighttime concentrations were $3.92 \times 10^7 \text{ cm}^{-3}$
17 for HO₂ and $1.64 \times 10^5 \text{ cm}^{-3}$ for OH. We compared the observed OH and HO₂
18 concentrations with those reported in previous studies conducted in urban, suburban,
19 rural forest, and coastal sites. As illustrated in Figure S5, the OH concentrations were
20 generally lower than those found in urban settings but similar to levels observed in
21 suburban, rural, and forest environments. This suggests a moderate level of
22 anthropogenic activity typical of mixed rural settings. In contrast, the HO₂
23 concentrations during these periods were significantly lower than earlier observations
24 in rural and forest environments, likely owing to reduced photochemical activity during
25 our measurement period.

26 **Table 1** Average concentrations and standard deviation of measured species throughout the entire
27 campaign (Total) and the selected 3 days cases from each cluster (PRD, CEC and CNC).

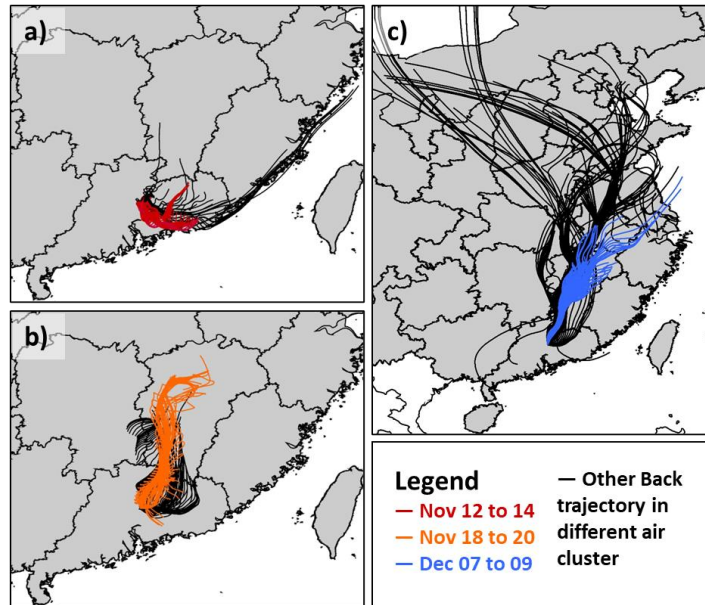
Species (Unit)	Total	PRD	CEC	CNC
AveMax OH _{Obs} 10 ⁶ (cm ⁻³)	3.5±2.5	6.9±1.1	4.9±1.5	5.3±0.9
OH _{Obs} 10 ⁶ (cm ⁻³)	0.9±1.5	1.6±2.2	1.4±1.6	1.2±1.8
OH _{DL} 10 ⁶ (cm ⁻³)	0.5±0.3	0.4±0.3	0.4±0.2	0.9±0.6
AveMax HO _{2 Obs} 10 ⁸ (cm ⁻³)	1.34±0.93	2.32±1.25	2.36±0.92	1.82±1.02
HO _{2 Obs} 10 ⁸ (cm ⁻³)	0.59±0.51	0.76±0.63	1.10±0.68	0.67±0.55
HO _{2 DL} 10 ⁸ (cm ⁻³)	0.19±0.11	0.17±0.10	0.25±0.08	0.26±0.15
Pressure (hpa)	995±4	992±1	992±1	995±2
Temp (°C)	16±6.1	23±3.0	23±2.6	14±2.8
RH (%)	78±15	87±11	86±10	81±9.4
Wind Speed (m/s)	0.91±0.65	0.53±0.32	0.57±0.34	0.87±0.5
j _{O1D} 10 ⁻⁶ (s ⁻¹)	3.2±5.4	3.5±6	3.6±5.9	4.0±6.6
j _{NO2} 10 ⁻³ (s ⁻¹)	1.3±1.9	1.3±2.1	1.4±2	1.6±2.3
HONO	0.169±0.104	0.249±0.084	0.201±0.070	0.133±0.033
SO ₂	0.5±0.8	0.5±0.6	0.4±0.5	0.4±0.5
NO ₂	4.89±2.37	6.25±2.47	4.84±2.23	4.52±1.97
NO	0.57±0.86	0.73±1.09	0.69±1.00	0.73±0.85
CO	557.36±225.92	739.41±153.84	464.73±74.34	513.36±22.02
Ozone	25±14	32±23	24±13	19±9.4
Particle Surface Area (um ² /cm ³)	86±72	186±51	84±28	48±19
Isoprene	0.082±0.174	0.257±0.337	0.155±0.200	0.029±0.030
*OVOCs	2.218±1.056	3.163±2.324	1.755±0.379	1.730±0.330
*AVOCs	8.346±3.223	9.662±5.031	6.886±1.755	6.801±0.864
*TEXs	0.356±0.316	0.801±0.616	0.266±0.090	0.237±0.085

1

2 Notes: Concentrations are expressed in parts per billion (ppb) unless otherwise specified. Total
 3 VOCs concentrations are categorized by origin (AVOCs, BVOCs, and OVOCs). For the average
 4 concentration of each measured VOCs, refer to Table S5.

5 Figure 4 illustrates the results of the 24-hour backward trajectory analysis,
 6 revealing three distinct but sequentially occurring phases. In the initial phase (Figure
 7 4a), air masses originated from the urban and industrial zones of the Pearl River Delta
 8 (PRD). This phase was characterised by intense photochemical activity, with ambient
 9 temperatures exceeding 20°C and relative humidity levels surpassing 70%. During this
 10 period, notably high concentrations of VOCs, ozone, and radicals were observed, with
 11 the average daily maximum concentrations of OH and HO₂ radicals reaching 6.50 ±
 12 1.19 × 10⁶ cm⁻³ and 2.20 ± 0.27 × 10⁸ cm⁻³, respectively. The subsequent phase was
 13 characterised by air masses originating from Central East China (CEC, Figure 4b). This
 14 phase showed reduced photochemical reactivity and lower concentrations of the
 15 measured trace gases. The average daily maximum concentrations of OH and HO₂
 16 during this phase were 4.35 ± 2.19 × 10⁶ cm⁻³ and 1.96 ± 0.90 × 10⁸ cm⁻³, respectively.
 17 The final phase was influenced by air masses from Central North China (CNC, Figure

1 4c), which exhibited the lowest concentrations of trace gases and the least pronounced
 2 average daily maximum concentrations in OH and HO₂ concentrations, measured at
 3 $2.23 \pm 1.95 \times 10^6 \text{ cm}^{-3}$ and $7.63 \pm 7.66 \times 10^7 \text{ cm}^{-3}$, respectively. This phase coincided
 4 with an increase in cloudy days and a decrease in temperatures, indicating reduced
 5 photochemical conditions.

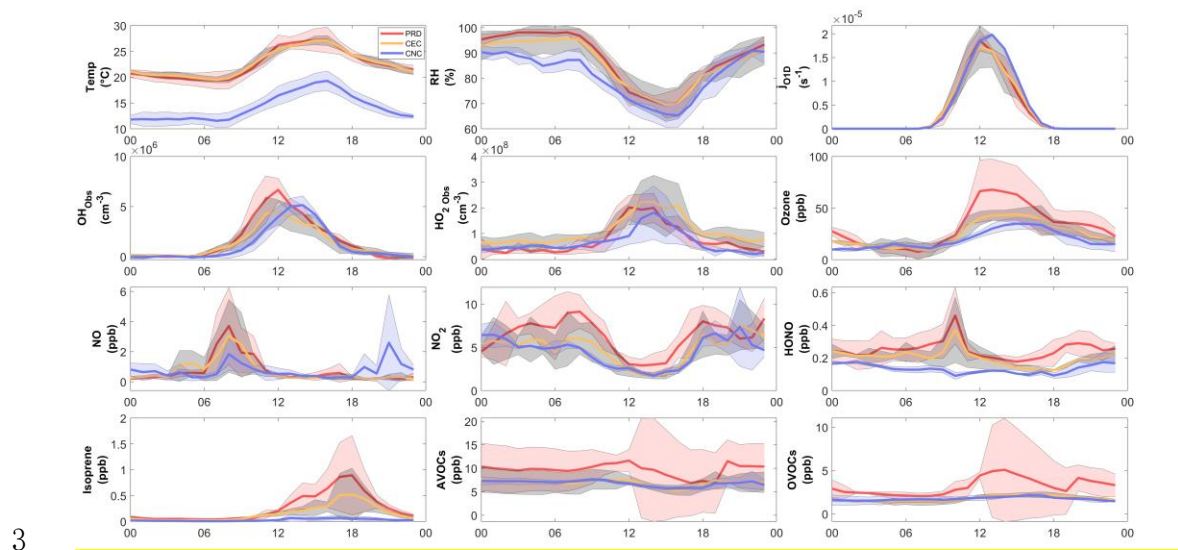


6
 7 **Figure 4** 24-hour back trajectories for (a) Pearl River Delta (5 days), (b) Central East China (4 days),
 8 and (c) Central North China (14 days) cases. Three days selected from each cluster for model
 9 simulation are distinguished by different colours.

10 3.1.2 Selection of Cases

11 For each phase, a representative three-day period was selected for detailed analysis
 12 based on the availability of comprehensive data and sunny conditions (colored
 13 trajectories in Figure 4). In the subsequent analysis, 'PRD,' 'CEC,' and 'CNC' refer to
 14 the selected periods corresponding to the air masses originating from these regions. The
 15 average daily maximum concentrations of OH and HO₂ radicals for these periods are
 16 presented in Table 1. The average daily max OH concentrations were $6.89 \pm 1.10 \times 10^6$
 17 cm^{-3} in PRD, $4.90 \pm 1.47 \times 10^6 \text{ cm}^{-3}$ in CEC, and $5.27 \pm 0.89 \times 10^6 \text{ cm}^{-3}$ in CNC, with
 18 a pronounce decrease from PRD to CEC (of $1.99 \times 10^6 \text{ cm}^{-3}$). The average daily max
 19 HO₂ concentrations were $2.32 \pm 1.25 \times 10^8 \text{ cm}^{-3}$ in PRD, $2.36 \pm 0.92 \times 10^8 \text{ cm}^{-3}$ in CEC,
 20 and $1.82 \pm 1.02 \times 10^8 \text{ cm}^{-3}$ in CNC, with a slight increase of $0.04 \times 10^8 \text{ cm}^{-3}$ from PRD

1 to CEC and a more substantial drop of $0.54 \times 10^8 \text{ cm}^{-3}$ from CEC to CNC. These trends
2 suggest a declining atmospheric oxidation capacity from PRD to CNC.



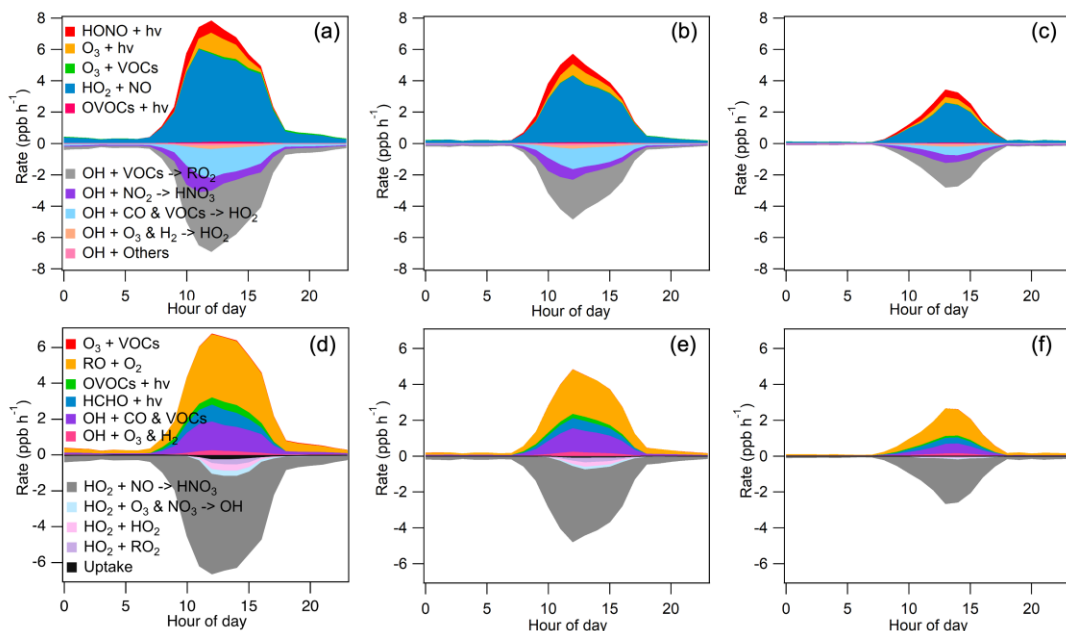
4 **Figure 5** Average diurnal variations of (a) Temperature (b) Relative Humidity (c) J_{OID} (d) OH
5 (e) HO₂ (f) Ozone (g) NO (h) NO₂ (i) HONO (j) Isoprene (k) AVOCs (l) OVOCs. The solid-colored
6 lines represent selected cases: orange for PRD, green for CEC, and blue for CNC. The light band
7 represents the standard deviations of the mean. The increase in the standard deviations of VOCs and
8 OVOCs during the PRD case is a result of absence of data on the afternoon of November 14th and
9 large variations in on November 12th and 13th.

10 The precursor concentrations and meteorological parameters also varied across
11 cases in terms of statistics (Tables 1 and S4) and diurnal variations (Figure 5). In the
12 PRD case, the average concentrations are characteristic of a rural environment, with
13 AVOCs at $9.70 \pm 5.00 \text{ ppb}$, OVOCs at $3.20 \pm 2.30 \text{ ppb}$, isoprene at $0.26 \pm 0.34 \text{ ppb}$, NO₂
14 at $6.3 \pm 2.5 \text{ ppb}$, and NO at $0.73 \pm 1.09 \text{ ppb}$. The NO concentration was affected by traffic
15 sources as no other fresh emission source nearby and the NO diurnal variation show a
16 morning peak in all three cases (Figure 5). In the CEC case, a general reduction in
17 anthropogenic influence is evident. AVOCs, OVOCs isoprene and NO₂ drop
18 significantly to $6.90 \pm 1.80 \text{ ppb}$, $1.70 \pm 0.38 \text{ ppb}$, 0.16 ± 0.20 and $4.84 \pm 2.23 \text{ ppb}$
19 respectively. Meanwhile, and NO remain close to PRD levels at $0.69 \pm 1.00 \text{ ppb}$. In the
20 CNC case, the air mass is more aged with reduced biogenic emissions, reflected in
21 further decreases in isoprene and NO₂ to $0.03 \pm 0.04 \text{ ppb}$ and $4.52 \pm 1.97 \text{ ppb}$, respectively,
22 due to colder weather conditions. The temperature decreased significantly from PRD

1 to CNC, whereas the average peak photolysis frequency was comparable between PRD
 2 and CNC, as shown in Table 1.

3 3.2 Chemical budgets of OH and HO₂

4 To investigate the OH and HO₂ chemical budgets during the three distinct periods,
 5 we employed a box model constrained by observed concentrations of NO_x, VOCs, and
 6 relevant meteorological parameters in the selected cases (base scenario which OH and
 7 HO₂ concentrations were not constrained by observation here). The resulting OH and
 8 HO₂ budgets, displaying typical bell-shaped patterns, are illustrated in Figure 6. During
 9 midday (10:00–15:00), the main source of HO₂ was the recycling of RO species, with
 10 rates of 3.22 ppb h⁻¹ for PRD, 2.09 ppb h⁻¹ for CEC, and 1.08 ppb h⁻¹ for CNC.
 11 Additionally, HCHO photolysis contributed 0.75 ppb h⁻¹, 0.46 ppb h⁻¹, and 0.26 ppb
 12 h⁻¹ for PRD, CEC, and CNC, respectively. The sinks of HO₂ varied among the cases
 13 with minor contribution from the uptake process, driven by radical termination
 14 mechanisms. The rate of radical self-reactions decreased from PRD to CNC. In contrast,
 15 NO_x-radical reactions between CEC and CNC were comparable, with respective rates
 16 of 0.39 ppb h⁻¹, and 0.33 ppb h⁻¹, indicating a shift in radical termination mechanisms.



17
 18 **Figure 6** Chemical budgets of OH and HO₂ for PRD (a, d), CEC (b, e), and CNC (c, f) simulated
 19 using a chemical box model.

1 OH formation was predominantly driven by the $\text{HO}_2 + \text{NO}$ reaction, contributing
2 5.18 ppb h^{-1} , 3.51 ppb h^{-1} , and 1.81 ppb h^{-1} (average for 10:00 – 15:00, hereafter in
3 this section) for PRD, CEC, and CNC, respectively. Additionally, contributions from
4 ozone photolysis and HONO increased from PRD to CEC and then to CNC, with rates
5 of 21.4%, 22.7%, and 24.6%, respectively. The primary sinks for OH included reactions
6 with VOCs to produce RO_2 , with rates of 3.31 ppb h^{-1} , 2.02 ppb h^{-1} , and 1.13 ppb h^{-1} ,
7 and reactions with CO and other VOCs to generate HO_2 , contributing 1.55 ppb h^{-1} , 1.06
8 ppb h^{-1} , and 0.38 ppb h^{-1} for PRD, CEC, and CNC, respectively. These findings
9 highlight the critical role of OH + VOC reactions in the chemical budget of OH.

10 **3.3 Comparison of model with observation results**

11 The modeled and observed concentrations of OH and HO_2 radicals were compared
12 to evaluate the performance of the model. In the PRD case (Figure 7), which is the most
13 polluted and warmest among the three cases, the OH concentration was only slightly
14 overestimated, whereas the HO_2 concentration was substantially overpredicted by the
15 model during the daytime. Similar result has been observed at another rural site
16 (Kanaya et al., 2012). For the CEC case (Figure 8), the model moderately overestimated
17 both radicals during the daytime but underestimated the nighttime HO_2 concentration,
18 which is similar to the findings at a rural forest site (Bottorff et al., 2023). In the CNC
19 case (Figure 9), the model results were generally within the measurement uncertainty,
20 with some daytime overestimation of HO_x on December 7 (similar to the PRD case)
21 and nighttime underestimation of HO_2 (similar to the CEC case). In the following
22 section, we conduct sensitivity tests to explore the possible reasons for the model
23 observation discrepancy in the PRD and CEC cases.

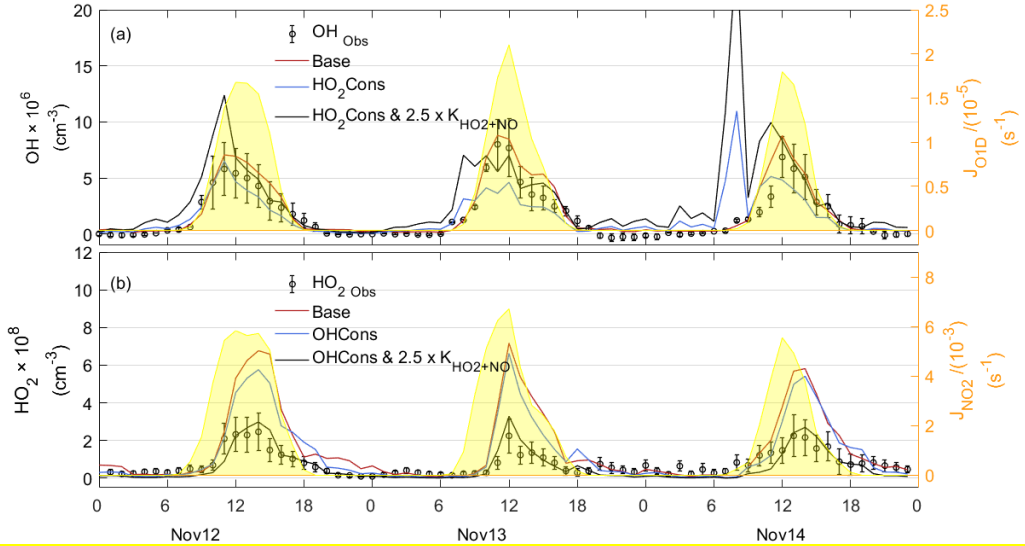


Figure 7 observed and simulated time series of OH and HO_2 for the PRD case. The “Obs” subscript denotes the observation data. “Base” denotes the result of Baseline scenario as described in Box Model section. “Cons” denotes the results with additional constrained species compared to Base. “ $2.5 \times K_{\text{HO}2+\text{NO}}$ ” denotes the results with increasing the reaction rate coefficient of R11 by a factor of 2.5.

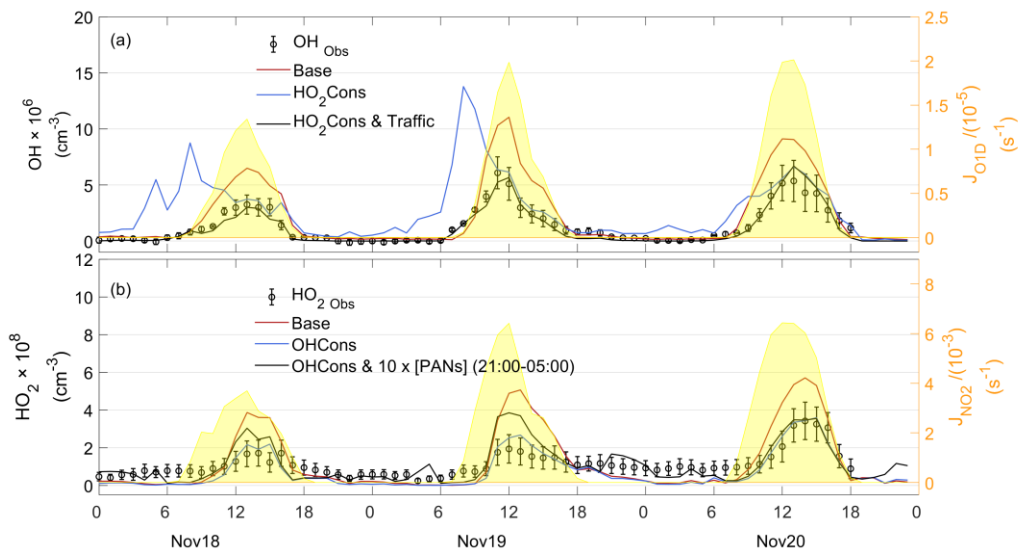
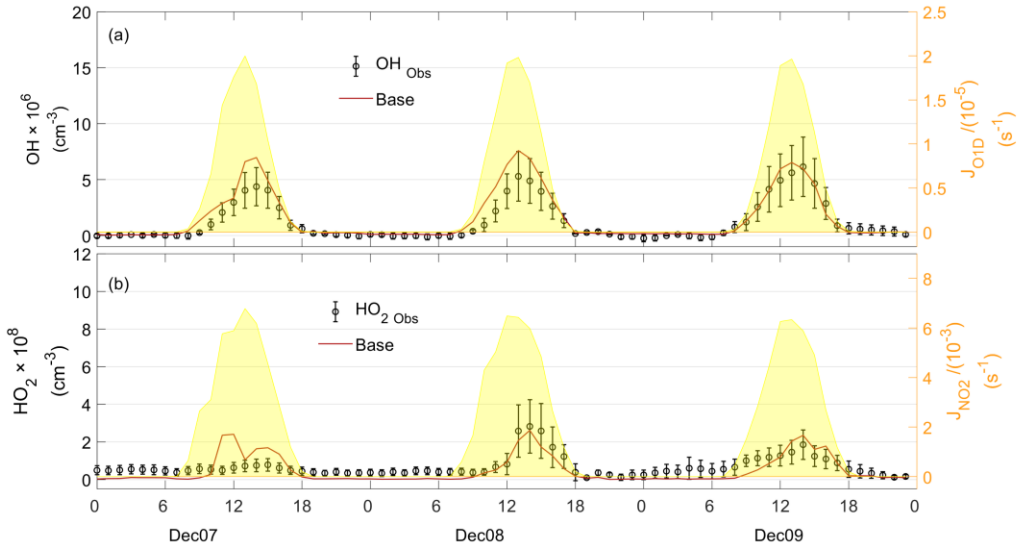


Figure 8 observed and simulated time series of OH and HO_2 for the CEC case. The “Obs” subscript denotes the observation data. “Base” denotes the result of Baseline scenario as described in Box Model section. “Cons” denotes the results with additional constrained species compared to Base. “Traffic” denotes the sensitivity test results with consideration of vehicular emission (see Test S7 in SI). “ $10 \times [\text{PANs}] (21:00-05:00)$ ” denotes the results with increasing nighttime secondary concentration of PAN by a factor of 10.



1 **Figure 9** observed and simulated time series of OH and HO₂ for the CNC case. “Base” denotes the
 2 result of Baseline scenario as described in Box Model section.
 3

4 **3.3.1 Substantial overestimation of HO₂ in PRD case**

5 To explain the HO₂ over-simulation by the base model, we constrain OH or HO₂
 6 and compared to the base case (without constraining OH and HO₂). Result shows that
 7 constraining HO₂ causes the model to underestimate OH (blue line in Figure 7a), while
 8 constraining OH leads the model to still substantially overestimate HO₂ (blue line in
 9 Figure 7b). This result suggests that aligning the modeled OH and HO₂ with
 10 observations may require introducing a strong, unknown process for HO₂ that
 11 efficiently recycles OH with a high yield (Kanaya et al., 2012). A sensitivity analysis
 12 shows that increasing the reaction rate coefficient of HO₂ + NO \rightarrow OH + NO₂ (R11)
 13 by a factor of 2.5 would largely reduce both the HO₂ overestimation and the OH
 14 underestimation as shown by the black line in Figure 7. However, it is not clear what
 15 such OH cycling reaction is. Thus, the exact cause of the overestimation of HO₂ in the
 16 PRD case remain unresolved.

17 **3.3.2 Moderate overestimation of both OH and HO₂ radicals in CEC case**

18 Unlike the PRD case, constraining either OH or HO₂ in the CEC case generally
 19 reduces the daytime overestimation of both HO₂ and OH. These results indicate an
 20 additional sink for both OH and HO₂, as suggested by Bottorff et al. (2023). However,
 21 the OH concentration shows an overestimation in the morning when HO₂ was
 22 constrained, which may suggest missing OH reactivity in the morning. To further

1 investigate the underlying causes, we examined the correlations between various
2 pollutants. The significant negative correlation between CO and NO ($R^2=0.49$, $p=0.01$,
3 Figure S6b) suggests that CEC in the morning may have been influenced by emission
4 from fresh complete combustion during the CEC case, whereas such correlations for
5 PRD and CNC are not significant (Figure S6a and c). This indicates that the missing
6 OH reactivity of CEC in the morning is possibly related to fresh vehicle emissions.

7 Diesel vehicle exhausts are rich in OVOCs relative to total VOCs (Yang et al.,
8 2023). In our study, OVOCs were measured, except formaldehyde and acetaldehyde.
9 We conducted a sensitivity analysis by adding these two OVOCs in the model (see Text
10 S7 for details). After accounting for their influence, the overestimation of OH in the
11 morning with constraining HO₂ could be significantly reduced (Figure 8a black line).

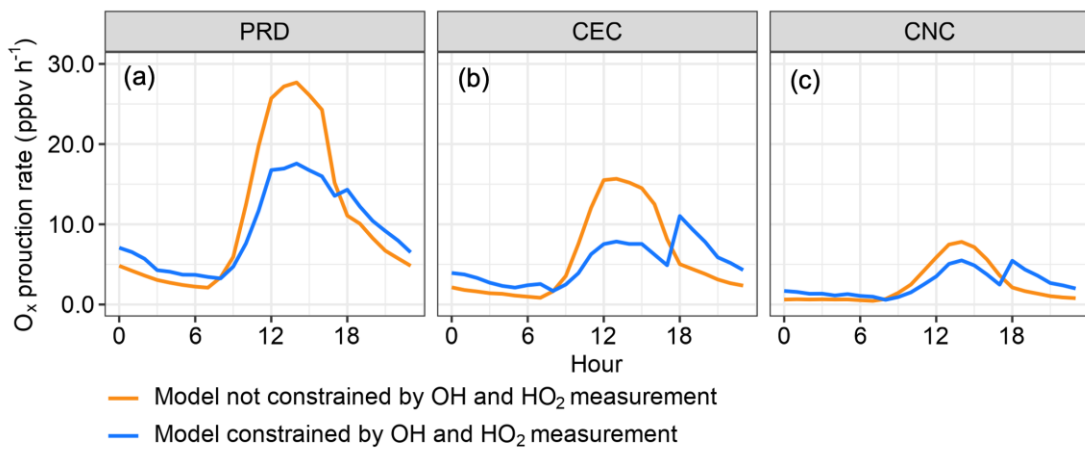
12 **3.3.3 Nighttime underestimation of HO₂ in CEC case**

13 Ozone and NO₃ reactions with alkenes can produce HO₂ at night (Walker et al.,
14 2015). In our study, alkenes are unlikely to be the main cause for the underestimation
15 because the major alkenes were measured, and the alkenes concentrations in the CEC
16 case were much lower compared to the PRD case in which no underestimation of
17 nighttime HO₂ was found. A previous study (Whalley et al., 2010) showed that
18 nighttime HO₂ underestimation at a clean tropical Atlantic site was significantly
19 reduced by constraining the model with higher PAN. In our study, PAN was not
20 measured. The model simulated nighttime PAN mixing ratios (0.1-0.7 ppb) were lower
21 than previous observed nighttime results in the coastal (up to 1 ppb) (Xu et al., 2015)
22 and mountain site (up to 2 ppb) (Wang et al., 2023) in southern China. To assess the
23 impact of PAN concentration on nighttime HO₂ levels, a sensitivity analysis was
24 conducted in which the PAN concentration was increased. The results show that only
25 when the PAN concentrations were increased by tenfold, the model simulated nighttime
26 PAN level could match the observations (Figure 8b, black line). This suggests that
27 underestimated PAN might have contributed to the model's nighttime HO₂
28 underestimation, but other processes must have a larger contribution.

29 **4. Implication for model overestimation of HO_x**

1 OH and HO₂ are key species that determine the atmosphere's oxidative processes.
 2 Inaccurate modelling of their sinks can lead to significant overestimation of oxidation
 3 capacity, resulting in skewed assessments of the impact of HO_x on air pollution and
 4 climate change. This problem is particularly pronounced in the case of ozone, a
 5 widespread photochemical pollutant. To demonstrate this issue, we compared
 6 simulation results from two modelling scenarios: the first scenario was constrained by
 7 observational parameters except OH and HO₂ (as described in section 3.2), while the
 8 second scenario included constraints from all observational parameters, including OH
 9 and HO₂ measurements.

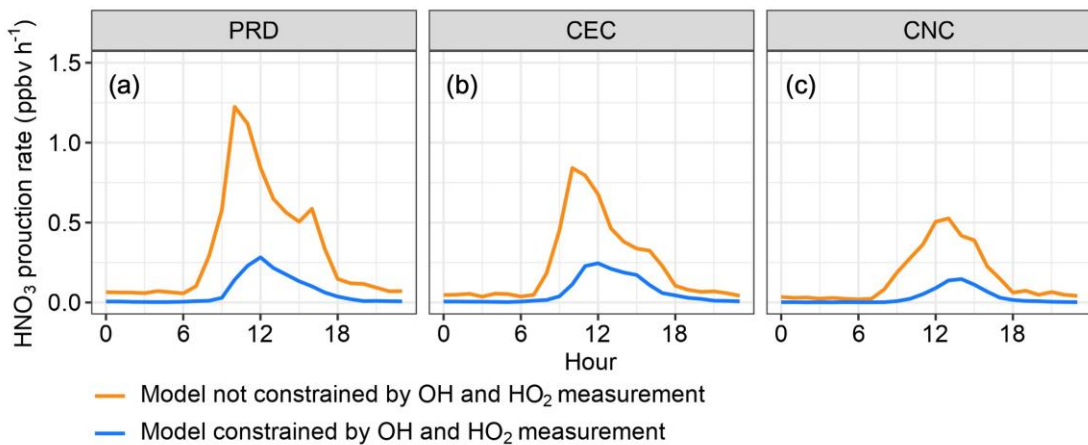
10 As illustrated in Figure 10, not constraining free-radical measurement data in the
 11 chemical model (the red line) led to overestimates of ozone's photochemical production
 12 rates. In the PRD case, simulated midday O_x (O₃ + NO₂) formation rates were
 13 overestimated by 59 % on average and 57% at peak values. In the CEC case, the
 14 overestimation was 98% on average and 91% at peak O_x rates, while the CNC case
 15 exhibited the smallest overestimation, 52% on average and 25% at peak values.



16
 17 **Figure 10** O_x (O₃+NO₂) photochemical production rates in three comparative cases: (a) PRD, (b)
 18 CEC, and (c) CNC. The red lines represent rates modelled with constraints on all observed data
 19 except OH and HO₂, while the green lines include constraints on all data, including OH and HO₂.

20 The overestimation of HO_x also significantly affected the simulated concentration
 21 of nitric acid (HNO₃), which is crucial for new particle formation and growth (Wang et
 22 al., 2020). Figure 11 illustrates that the chemical model drastically overestimated nitric
 23 acid production rates without constraints of free-radical measurements (the orange line).

1 The midday production rates of nitric acid were overestimated by factors of 3.16, 2.02,
 2 and 3.41 in the PRD, CEC, and CNC cases, respectively. Such overestimations can
 3 considerably impact assessments of new particle formation and growth processes and
 4 their impact on air pollution and climate change.



5 **Figure 11** Modelled HNO_3 production rates in three comparative cases: (a) PRD, (b) CEC, and (c)
 6 CNC. The red lines represent rates modelled with constraints on all observed data except OH and
 7 HO_2 , while the green lines include constraints on all data, including OH and HO_2 .

9 5. Conclusion

10 HO_2 and OH concentrations were measured using a chemical ionization mass
 11 spectrometer at a subtropical rural site in southern China from 12 November to 19
 12 December 2022. The measurements indicated generally lower concentrations of OH
 13 and HO_2 than those observed in previous studies at various sites. Backward trajectory
 14 analysis revealed three distinct phases characterised by sequentially decreasing
 15 pollution levels and temperatures. During the cold, clean period, model simulations
 16 closely matched the observed OH and HO_2 concentrations. However, during the warm,
 17 polluted period, the models overestimated HO_2 or both radicals. **Model sensitivity**
 18 **analysis indicates that adding an OH cycling reaction from HO_2 or additional sinks of**
 19 **OH and HO_2 would largely reduce the model-observation discrepancy in different cases**
 20 **of this study. However, the exact chemical reactions remain to be identified. Our results**
 21 **are in line with previous studies indicating substantial gaps in our understanding of the**
 22 **sources and sinks of OH and HO_2 in certain environments. Our study provides**
 23 **additional evidence for current incomplete understanding of the HO_x sources or sinks**

1 and calls for more research to resolve the model–observation mismatch found in this
2 work and previous studies.

3 The over-prediction of HO_x resulted in significant over simulation of the production
4 rates of other secondary pollutants such as ozone and nitric acid at the site. It is critical
5 to evaluate the capability of OH and HO₂ simulations in major chemical transport
6 models and earth system models as inaccurate simulations of OH and HO₂ may
7 misguide the development of air pollution and global warming control strategies.

8 **Data availability.** All of the data used to produce this paper can be obtained by
9 contacting Tao Wang (tao.wang@polyu.edu.hk).

10 **Supplement.** The online supplement for this article is available at:

11 **Author contributions.** TW conceived the HO_x research. TW, XW and YZ planned and
12 organized the overall field campaign at Conghua. ZZ conducted the OH measurements
13 using CIMS, with contributions from TW and WS, QC, and SH. XF, ZR, XL, AG, QW,
14 CP, and XT performed the JNO₂ VOCs and OVOCs measurements. ZZ performed the
15 chemical box modelling with contributions from TC and QC. TC, ZZ, and TW analysed
16 the data and interpreted the result (ZZ analysed the time series and diurnal variations of
17 observation data; TC interpreted the results of box model, investigated the missing
18 sources; TW supervised and guided these processes). TC, ZZ, and TW wrote the paper.
19 All of the authors reviewed and commented on the paper.

20 **Competing interests.** One author (Tao Wang) is a member of the editorial board of
21 Atmospheric Chemistry and Physics. The authors have no other competing interests to
22 declare.

23 **Acknowledgments**

24 We thank David Tanner, Dr. Wei Pu, Dr. Weihao Wang, and Dr. Zhe Wang for
25 developing the PolyU-CIMS. We are also grateful to the Guangzhou Institute of
26 Geochemistry, Chinese Academy of Sciences, for providing access to its station and
27 data on trace gases.

1 **Financial support.**

2 This research was financially supported by the Hong Kong Research Grants Council
3 (T24-504/17-N and 15223221 to Tao Wang), the National Science Foundation of China
4 (42293322 to Tao Wang), and The Hong Kong Polytechnic University Postdoc
5 Matching Fund Scheme (P0043403 to Tianshu Chen).

6 **Reference**

7 Berresheim, H., Elste, T., Tremmel, H. G., Allen, A. G., Hansson, H.-C., Rosman, K., Dal Maso,
8 M., Mäkelä, J. M., Kulmala, M., and O'Dowd, C. D.: Gas-aerosol relationships of H_2SO_4 , MSA,
9 and OH: Observations in the coastal marine boundary layer at Mace Head, Ireland, *Journal of*
10 *Geophysical Research: Atmospheres*, 107, PAR 5-1-PAR 5-12,
11 <https://doi.org/10.1029/2000JD000229>, 2002.

12 Bottorff, B., Lew, M. M., Woo, Y., Rickly, P., Rollings, M. D., Deming, B., Anderson, D. C., Wood,
13 E., Alwe, H. D., Millet, D. B., Weinheimer, A., Tyndall, G., Ortega, J., Dusanter, S., Leonardis, T.,
14 Flynn, J., Erickson, M., Alvarez, S., Rivera-Rios, J. C., Shutter, J. D., Keutsch, F., Helmig, D., Wang,
15 W., Allen, H. M., Slade, J. H., Shepson, P. B., Bertman, S., and Stevens, P. S.: OH, HO_2 , and RO_2
16 radical chemistry in a rural forest environment: measurements, model comparisons, and
17 evidence of a missing radical sink, *Atmospheric Chemistry and Physics*, 23, 10287–10311,
18 <https://doi.org/10.5194/acp-23-10287-2023>, 2023.

19 Carslaw, N., Creasey, D. J., Heard, D. E., Lewis, A. C., McQuaid, J. B., Pilling, M. J., Monks, P. S.,
20 Bandy, B. J., and Penkett, S. A.: Modeling OH, HO_2 , and RO_2 radicals in the marine boundary
21 layer: 1. Model construction and comparison with field measurements, *J. Geophys. Res.*, 104,
22 30241–30255, <https://doi.org/10.1029/1999JD900783>, 1999.

23 Chen, Q., Xia, M., Peng, X., Yu, C., Sun, P., Li, Y., Liu, Y., Xu, Z., Xu, Z., Wu, R., Nie, W., Ding, A.,
24 Zhao, Y., and Wang, T.: Large Daytime Molecular Chlorine Missing Source at a Suburban Site
25 in East China, *JGR Atmospheres*, 127, <https://doi.org/10.1029/2021JD035796>, 2022.

26 Edwards, G. D., Cantrell, C. A., Stephens, S., Hill, B., Goyea, O., Shetter, R. E., Mauldin, R. L.,
27 Kosciuch, E., Tanner, D. J., and Eisele, F. L.: Chemical Ionization Mass Spectrometer Instrument
28 for the Measurement of Tropospheric HO_2 and RO_2 , *Anal. Chem.*, 75, 5317–5327,
29 <https://doi.org/10.1021/ac034402b>, 2003.

30 Eisele, F. L. and Tanner, D. J.: Ion-assisted tropospheric OH measurements, *J. Geophys. Res.*,
31 96, 9295, <https://doi.org/10.1029/91JD00198>, 1991.

32 Eisele, F. L. and Tanner, D. J.: Measurement of the gas phase concentration of H_2SO_4 and
33 methane sulfonic acid and estimates of H_2SO_4 production and loss in the atmosphere, *Journal*
34 *of Geophysical Research: Atmospheres*, 98, 9001–9010, <https://doi.org/10.1029/93JD00031>,
35 1993.

1 Feiner, P. A., Brune, W. H., Miller, D. O., Zhang, L., Cohen, R. C., Romer, P. S., Goldstein, A. H.,
2 Keutsch, F. N., Skog, K. M., Wennberg, P. O., Nguyen, T. B., Teng, A. P., DeGouw, J., Koss, A.,
3 Wild, R. J., Brown, S. S., Guenther, A., Edgerton, E., Baumann, K., and Fry, J. L.: Testing
4 Atmospheric Oxidation in an Alabama Forest, *Journal of the Atmospheric Sciences*, 73, 4699–
5 4710, <https://doi.org/10.1175/JAS-D-16-0044.1>, 2016.

6 Fuchs, H., Bohn, B., Hofzumahaus, A., Holland, F., Lu, K. D., Nehr, S., Rohrer, F., and Wahner,
7 A.: Detection of HO₂ by laser-induced fluorescence: calibration and interferences from RO₂
8 radicals, *Atmospheric Measurement Techniques*, 4, 1209–1225, <https://doi.org/10.5194/amt-4-1209-2011>, 2011.

10 Fuchs, H., Acir, I.-H., Bohn, B., Brauers, T., Dorn, H.-P., Häseler, R., Hofzumahaus, A., Holland,
11 F., Kaminski, M., Li, X., Lu, K., Lutz, A., Nehr, S., Rohrer, F., Tillmann, R., Wegener, R., and Wahner,
12 A.: OH regeneration from methacrolein oxidation investigated in the atmosphere simulation
13 chamber SAPHIR, *Atmos. Chem. Phys.*, 14, 7895–7908, <https://doi.org/10.5194/acp-14-7895-2014>, 2014.

15 Griffith, S. M., Hansen, R. F., Dusanter, S., Stevens, P. S., Alaghmand, M., Bertman, S. B., Carroll,
16 M. A., Erickson, M., Galloway, M., Grossberg, N., Hottle, J., Hou, J., Jobson, B. T., Kammrath, A.,
17 Keutsch, F. N., Lefer, B. L., Mielke, L. H., O'Brien, A., Shepson, P. B., Thurlow, M., Wallace, W.,
18 Zhang, N., and Zhou, X. L.: OH and HO₂ radical chemistry during PROPHET 2008 and CABINEX
19 2009 – Part 1: Measurements and model comparison, *Atmospheric Chemistry and Physics*, 13,
20 5403–5423, <https://doi.org/10.5194/acp-13-5403-2013>, 2013.

21 Guo, J., Wang, Z., Tao Wang, and Zhang, X.: Theoretical evaluation of different factors
22 affecting the HO₂ uptake coefficient driven by aqueous-phase first-order loss reaction,
23 *Science of The Total Environment*, 683, 146–153,
24 <https://doi.org/10.1016/j.scitotenv.2019.05.237>, 2019.

25 Hanke, M., Uecker, J., Reiner, T., and Arnold, F.: Atmospheric peroxy radicals: ROXMAS, a new
26 mass-spectrometric methodology for speciated measurements of HO₂ and \sum RO₂ and first
27 results, *International Journal of Mass Spectrometry*, 213, 91–99,
28 [https://doi.org/10.1016/S1387-3806\(01\)00548-6](https://doi.org/10.1016/S1387-3806(01)00548-6), 2002.

29 Hansen, R. F., Griffith, S. M., Dusanter, S., Rickly, P. S., Stevens, P. S., Bertman, S. B., Carroll, M.
30 A., Erickson, M. H., Flynn, J. H., Grossberg, N., Jobson, B. T., Lefer, B. L., and Wallace, H. W.:
31 Measurements of total hydroxyl radical reactivity during CABINEX 2009 – Part 1: field
32 measurements, *Atmos. Chem. Phys.*, 14, 2923–2937, <https://doi.org/10.5194/acp-14-2923-2014>, 2014.

34 Heard, D. E. and Pilling, M. J.: Measurement of OH and HO₂ in the Troposphere, *Chem. Rev.*,
35 103, 5163–5198, <https://doi.org/10.1021/cr020522s>, 2003.

36 Hens, K., Novelli, A., Martinez, M., Auld, J., Axinte, R., Bohn, B., Fischer, H., Keronen, P., Kubistin,
37 D., Nölscher, A. C., Oswald, R., Paasonen, P., Petäjä, T., Regelin, E., Sander, R., Sinha, V., Sipilä,
38 M., Taraborrelli, D., Tatum Ernest, C., Williams, J., Lelieveld, J., and Harder, H.: Observation and

1 modelling of HO_x radicals in a boreal forest, *Atmospheric Chemistry and Physics*, 14, 8723–
2 8747, <https://doi.org/10.5194/acp-14-8723-2014>, 2014.

3 Hofzumahaus, A., Rohrer, F., Lu, K., Bohn, B., Brauers, T., Chang, C.-C., Fuchs, H., Holland, F.,
4 Kita, K., Kondo, Y., Li, X., Lou, S., Shao, M., Zeng, L., Wahner, A., and Zhang, Y.: Amplified Trace
5 Gas Removal in the Troposphere, *Science*, 324, 1702–1704,
6 <https://doi.org/10.1126/science.1164566>, 2009.

7 Jacob, D.: Heterogeneous chemistry and tropospheric ozone, *Atmospheric Environment*, 34,
8 2131–2159, [https://doi.org/10.1016/S1352-2310\(99\)00462-8](https://doi.org/10.1016/S1352-2310(99)00462-8), 2000.

9 Jeong, D., Seco, R., Emmons, L., Schwantes, R., Liu, Y., McKinney, K. A., Martin, S. T., Keutsch,
10 F. N., Gu, D., Guenther, A. B., Vega, O., Tota, J., Souza, R. A. F., Springston, S. R., Watson, T. B.,
11 and Kim, S.: Reconciling Observed and Predicted Tropical Rainforest OH Concentrations, *JGR
Atmospheres*, 127, <https://doi.org/10.1029/2020JD032901>, 2022.

13 Kanaya, Y., Cao, R., Kato, S., Miyakawa, Y., Kajii, Y., Tanimoto, H., Yokouchi, Y., Mochida, M.,
14 Kawamura, K., and Akimoto, H.: Chemistry of OH and HO₂ radicals observed at Rishiri Island,
15 Japan, in September 2003: Missing daytime sink of HO₂ and positive nighttime correlations
16 with monoterpenes, *J. Geophys. Res.*, 112, D11308, <https://doi.org/10.1029/2006JD007987>,
17 2007.

18 Kim, S., Wolfe, G. M., Mauldin, L., Cantrell, C., Guenther, A., Karl, T., Turnipseed, A., Greenberg,
19 J., Hall, S. R., Ullmann, K., Apel, E., Hornbrook, R., Kajii, Y., Nakashima, Y., Keutsch, F. N., DiGangi,
20 J. P., Henry, S. B., Kaser, L., Schnitzhofer, R., Graus, M., Hansel, A., Zheng, W., and Flocke, F. F.:
21 Evaluation of HO_x sources and cycling using measurement-constrained model calculations in
22 a 2-methyl-3-butene-2-ol (MBO) and monoterpene (MT) dominated ecosystem,
23 *Atmospheric Chemistry and Physics*, 13, 2031–2044, <https://doi.org/10.5194/acp-13-2031-2013>, 2013.

25 Kürten, A., Rondo, L., Ehrhart, S., and Curtius, J.: Calibration of a Chemical Ionization Mass
26 Spectrometer for the Measurement of Gaseous Sulfuric Acid, *J. Phys. Chem. A*, 116, 6375–
27 6386, <https://doi.org/10.1021/jp212123n>, 2012.

28 Lelieveld, J., Butler, T. M., Crowley, J. N., Dillon, T. J., Fischer, H., Ganzeveld, L., Harder, H.,
29 Lawrence, M. G., Martinez, M., Taraborrelli, D., and Williams, J.: Atmospheric oxidation capacity
30 sustained by a tropical forest, *Nature*, 452, 737–740, <https://doi.org/10.1038/nature06870>,
31 2008.

32 Lew, M. M., Rickly, P. S., Bottorff, B. P., Reidy, E., Sklaveniti, S., Léonardis, T., Locoge, N.,
33 Dusanter, S., Kundu, S., Wood, E., and Stevens, P. S.: OH and HO₂ radical chemistry in a
34 midlatitude forest: measurements and model comparisons, *Atmospheric Chemistry and
35 Physics*, 20, 9209–9230, <https://doi.org/10.5194/acp-20-9209-2020>, 2020.

36 Lou, S., Holland, F., Rohrer, F., Lu, K., Bohn, B., Brauers, T., Chang, C. C., Fuchs, H., Häseler, R.,
37 Kita, K., Kondo, Y., Li, X., Shao, M., Zeng, L., Wahner, A., Zhang, Y., Wang, W., and Hofzumahaus,

1 A.: Atmospheric OH reactivities in the Pearl River Delta – China in summer 2006: measurement
2 and model results, *Atmos. Chem. Phys.*, 10, 11243–11260, <https://doi.org/10.5194/acp-10-11243-2010>, 2010.

4 Ma, X., Tan, Z., Lu, K., Yang, X., Liu, Y., Li, S., Li, X., Chen, S., Novelli, A., Cho, C., Zeng, L., Wahner,
5 A., and Zhang, Y.: Winter photochemistry in Beijing: Observation and model simulation of OH
6 and HO₂ radicals at an urban site, *Science of The Total Environment*, 685, 85–95,
7 <https://doi.org/10.1016/j.scitotenv.2019.05.329>, 2019.

8 Ma, X., Tan, Z., Lu, K., Yang, X., Chen, X., Wang, H., Chen, S., Fang, X., Li, S., Li, X., Liu, J., Liu, Y.,
9 Lou, S., Qiu, W., Wang, H., Zeng, L., and Zhang, Y.: OH and HO₂ radical chemistry at a suburban
10 site during the EXPLORE-YRD campaign in 2018, *Atmospheric Chemistry and Physics*, 22,
11 7005–7028, <https://doi.org/10.5194/acp-22-7005-2022>, 2022.

12 Mallik, C., Tomsche, L., Bourtsoukidis, E., Crowley, J. N., Derstroff, B., Fischer, H., Hafermann,
13 S., Hüser, I., Javed, U., Keßel, S., Lelieveld, J., Martinez, M., Meusel, H., Novelli, A., Phillips, G. J.,
14 Pozzer, A., Reiffs, A., Sander, R., Taraborrelli, D., Sauvage, C., Schuladen, J., Su, H., Williams, J.,
15 and Harder, H.: Oxidation processes in the eastern Mediterranean atmosphere: evidence from
16 the modelling of HO_x measurements over Cyprus, *Atmospheric Chemistry and Physics*, 18,
17 10825–10847, <https://doi.org/10.5194/acp-18-10825-2018>, 2018.

18 Mao, J., Ren, X., Zhang, L., Van Duin, D. M., Cohen, R. C., Park, J.-H., Goldstein, A. H., Paulot,
19 F., Beaver, M. R., Crounse, J. D., Wennberg, P. O., DiGangi, J. P., Henry, S. B., Keutsch, F. N.,
20 Park, C., Schade, G. W., Wolfe, G. M., Thornton, J. A., and Brune, W. H.: Insights into hydroxyl
21 measurements and atmospheric oxidation in a California forest, *Atmos. Chem. Phys.*, 12,
22 8009–8020, <https://doi.org/10.5194/acp-12-8009-2012>, 2012.

23 Mauldin III, R. L., Kosciuch, E., Henry, B., Eisele, F. L., Shetter, R., Lefer, B., Chen, G., Davis, D.,
24 Huey, G., and Tanner, D.: Measurements of OH, HO₂+RO₂, H₂SO₄, and MSA at the South Pole
25 during ISCAT 2000, *Atmospheric Environment*, 38, 5423–5437,
26 <https://doi.org/10.1016/j.atmosenv.2004.06.031>, 2004.

27 Muller, J. B. A., Elste, T., Plass-Dülmer, C., Stange, G., Holla, R., Claude, A., Englert, J., Gilge, S.,
28 and Kubistin, D.: A novel semi-direct method to measure OH reactivity by chemical ionization
29 mass spectrometry (CIMS), *Atmos. Meas. Tech.*, 11, 4413–4433, <https://doi.org/10.5194/amt-11-4413-2018>, 2018.

31 Novelli, A., Hens, K., Tatum Ernest, C., Kubistin, D., Regelin, E., Elste, T., Plass-Dülmer, C.,
32 Martinez, M., Lelieveld, J., and Harder, H.: Characterisation of an inlet pre-injector laser-
33 induced fluorescence instrument for the measurement of atmospheric hydroxyl radicals,
34 *Atmos. Meas. Tech.*, 7, 3413–3430, <https://doi.org/10.5194/amt-7-3413-2014>, 2014.

35 Novelli, A., Vereecken, L., Bohn, B., Dorn, H.-P., Gkatzelis, G. I., Hofzumahaus, A., Holland, F.,
36 Reimer, D., Rohrer, F., Rosanka, S., Taraborrelli, D., Tillmann, R., Wegener, R., Yu, Z., Kiendler-
37 Scharr, A., Wahner, A., and Fuchs, H.: Importance of isomerization reactions for OH radical
38 regeneration from the photo-oxidation of isoprene investigated in the atmospheric

1 simulation chamber SAPHIR, Atmos. Chem. Phys., 20, 3333–3355,
2 <https://doi.org/10.5194/acp-20-3333-2020>, 2020.

3 Sjostedt, S. J., Huey, L. G., Tanner, D. J., Peischl, J., Chen, G., Dibb, J. E., Lefer, B., Hutterli, M. A.,
4 Beyersdorf, A. J., Blake, N. J., Blake, D. R., Sueper, D., Ryerson, T., Burkhardt, J., and Stohl, A.:
5 Observations of hydroxyl and the sum of peroxy radicals at Summit, Greenland during
6 summer 2003, Atmospheric Environment, 41, 5122–5137,
7 <https://doi.org/10.1016/j.atmosenv.2006.06.065>, 2007.

8 Slater, E. J., Whalley, L. K., Woodward-Massey, R., Ye, C., Lee, J. D., Squires, F., Hopkins, J. R.,
9 Dunmore, R. E., Shaw, M., Hamilton, J. F., Lewis, A. C., Crilley, L. R., Kramer, L., Bloss, W., Vu, T.,
10 Sun, Y., Xu, W., Yue, S., Ren, L., Acton, W. J. F., Hewitt, C. N., Wang, X., Fu, P., and Heard, D. E.:
11 Elevated levels of OH observed in haze events during wintertime in central Beijing,
12 Atmospheric Chemistry and Physics, 20, 14847–14871, <https://doi.org/10.5194/acp-20-14847-2020>, 2020.

14 Stone, D., Whalley, L. K., and Heard, D. E.: Tropospheric OH and HO₂ radicals: field
15 measurements and model comparisons, Chem. Soc. Rev., 41, 6348,
16 <https://doi.org/10.1039/c2cs35140d>, 2012.

17 Tan, D., Faloona, I., Simpas, J. B., Brune, W., Shepson, P. B., Couch, T. L., Sumner, A. L., Carroll,
18 M. A., Thornberry, T., Apel, E., Riemer, D., and Stockwell, W.: HO_x budgets in a deciduous forest:
19 Results from the PROPHET summer 1998 campaign, J. Geophys. Res., 106, 24407–24427,
20 <https://doi.org/10.1029/2001JD900016>, 2001.

21 Tan, Z., Fuchs, H., Lu, K., Hofzumahaus, A., Bohn, B., Broch, S., Dong, H., Gomm, S., Häseler, R.,
22 He, L., Holland, F., Li, X., Liu, Y., Lu, S., Rohrer, F., Shao, M., Wang, B., Wang, M., Wu, Y., Zeng,
23 L., Zhang, Y., Wahner, A., and Zhang, Y.: Radical chemistry at a rural site (Wangdu) in the
24 North China Plain: observation and model calculations of OH, HO₂ and RO₂ radicals,
25 Atmospheric Chemistry and Physics, 17, 663–690, <https://doi.org/10.5194/acp-17-663-2017>,
26 2017.

27 Tan, Z., Rohrer, F., Lu, K., Ma, X., Bohn, B., Broch, S., Dong, H., Fuchs, H., Gkatzelis, G. I.,
28 Hofzumahaus, A., Holland, F., Li, X., Liu, Y., Liu, Y., Novelli, A., Shao, M., Wang, H., Wu, Y., Zeng,
29 L., Hu, M., Kiendler-Scharr, A., Wahner, A., and Zhang, Y.: Wintertime photochemistry in
30 Beijing: observations of RO_x radical concentrations in the North China Plain during the BEST-
31 ONE campaign, Atmospheric Chemistry and Physics, 18, 12391–12411,
32 <https://doi.org/10.5194/acp-18-12391-2018>, 2018.

33 Tan, Z., Lu, K., Hofzumahaus, A., Fuchs, H., Bohn, B., Holland, F., Liu, Y., Rohrer, F., Shao, M.,
34 Sun, K., Wu, Y., Zeng, L., Zhang, Y., Zou, Q., Kiendler-Scharr, A., Wahner, A., and Zhang, Y.:
35 Experimental budgets of OH, HO₂, and RO₂ radicals and implications for ozone formation in
36 the Pearl River Delta in China 2014, Atmospheric Chemistry and Physics, 19, 7129–7150,
37 <https://doi.org/10.5194/acp-19-7129-2019>, 2019.

38 Tanner, D. J. and Eisele, F. L.: Present OH measurement limits and associated uncertainties, J.

1 Geophys. Res., 100, 2883, <https://doi.org/10.1029/94JD02609>, 1995.

2 Tanner, D. J., Jefferson, A., and Eisele, F. L.: Selected ion chemical ionization mass
3 spectrometric measurement of OH, J. Geophys. Res., 102, 6415–6425,
4 <https://doi.org/10.1029/96JD03919>, 1997.

5 Thames, A. B., Brune, W. H., Miller, D. O., Allen, H. M., Apel, E. C., Blake, D. R., Bui, T. P.,
6 Commane, R., Crounse, J. D., Daube, B. C., Diskin, G. S., DiGangi, J. P., Elkins, J. W., Hall, S. R.,
7 Hanisco, T. F., Hannun, R. A., Hints, E., Hornbrook, R. S., Kim, M. J., McKain, K., Moore, F. L.,
8 Nicely, J. M., Peischl, J., Ryerson, T. B., St. Clair, J. M., Sweeney, C., Teng, A., Thompson, C. R.,
9 Ullmann, K., Wennberg, P. O., and Wolfe, G. M.: Missing OH reactivity in the global marine
10 boundary layer, Atmospheric Chemistry and Physics, 20, 4013–4029,
11 <https://doi.org/10.5194/acp-20-4013-2020>, 2020.

12 Wang, M., Kong, W., Marten, R., He, X.-C., Chen, D., Pfeifer, J., Heitto, A., Kontkanen, J., Dada,
13 L., Kürten, A., Yli-Juuti, T., Manninen, H. E., Amanatidis, S., Amorim, A., Baalbaki, R., Baccarini,
14 A., Bell, D. M., Bertozi, B., Bräkling, S., Brilke, S., Murillo, L. C., Chiu, R., Chu, B., De Menezes,
15 L.-P., Duplissy, J., Finkenzeller, H., Carracedo, L. G., Granzin, M., Guida, R., Hansel, A., Hofbauer,
16 V., Krechmer, J., Lehtipalo, K., Lamkaddam, H., Lampimäki, M., Lee, C. P., Makhmutov, V., Marie,
17 G., Mathot, S., Mauldin, R. L., Mentler, B., Müller, T., Onnela, A., Partoll, E., Petäjä, T., Philippov,
18 M., Pospisilova, V., Ranjithkumar, A., Rissanen, M., Rörup, B., Scholz, W., Shen, J., Simon, M.,
19 Sipilä, M., Steiner, G., Stolzenburg, D., Tham, Y. J., Tomé, A., Wagner, A. C., Wang, D. S., Wang,
20 Y., Weber, S. K., Winkler, P. M., Wlasits, P. J., Wu, Y., Xiao, M., Ye, Q., Zauner-Wieczorek, M.,
21 Zhou, X., Volkamer, R., Riipinen, I., Dommen, J., Curtius, J., Baltensperger, U., Kulmala, M.,
22 Worsnop, D. R., Kirkby, J., Seinfeld, J. H., El-Haddad, I., Flagan, R. C., and Donahue, N. M.:
23 Rapid growth of new atmospheric particles by nitric acid and ammonia condensation, Nature,
24 581, 184–189, <https://doi.org/10.1038/s41586-020-2270-4>, 2020.

25 Wang, X., Jacob, D. J., Eastham, S. D., Sulprizio, M. P., Zhu, L., Chen, Q., Alexander, B., Sherwen,
26 T., Evans, M. J., Lee, B. H., Haskins, J. D., Lopez-Hilfiker, F. D., Thornton, J. A., Huey, G. L., and
27 Liao, H.: The role of chlorine in global tropospheric chemistry, Atmospheric Chemistry and
28 Physics, 19, 3981–4003, <https://doi.org/10.5194/acp-19-3981-2019>, 2019.

29 Wang, Y., Liu, T., Gong, D., Wang, H., Guo, H., Liao, M., Deng, S., Cai, H., and Wang, B.:
30 Anthropogenic Pollutants Induce Changes in Peroxyacetyl Nitrate Formation Intensity and
31 Pathways in a Mountainous Background Atmosphere in Southern China, Environ. Sci. Technol.,
32 57, 6253–6262, <https://doi.org/10.1021/acs.est.2c02845>, 2023.

33 Wennberg, P. O., Bates, K. H., Crounse, J. D., Dodson, L. G., McVay, R. C., Mertens, L. A., Nguyen,
34 T. B., Praske, E., Schwantes, R. H., Smarte, M. D., St. Clair, J. M., Teng, A. P., Zhang, X., and
35 Seinfeld, J. H.: Gas-Phase Reactions of Isoprene and Its Major Oxidation Products, Chem. Rev.,
36 118, 3337–3390, <https://doi.org/10.1021/acs.chemrev.7b00439>, 2018.

37 Whalley, L. K., Edwards, P. M., Furneaux, K. L., Goddard, A., Ingham, T., Evans, M. J., Stone, D.,
38 Hopkins, J. R., Jones, C. E., Karunaharan, A., Lee, J. D., Lewis, A. C., Monks, P. S., Moller, S. J.,
39 and Heard, D. E.: Quantifying the magnitude of a missing hydroxyl radical source in a tropical

1 rainforest, *Atmos. Chem. Phys.*, 11, 7223–7233, <https://doi.org/10.5194/acp-11-7223-2011>,
2 2011.

3 Wolfe, G. M., Marvin, M. R., Roberts, S. J., Travis, K. R., and Liao, J.: The Framework for 0-D
4 Atmospheric Modeling (F0AM) v3.1, *Geosci. Model Dev.*, 9, 3309–3319,
5 <https://doi.org/10.5194/gmd-9-3309-2016>, 2016.

6 Woodward-Massey, R., Slater, E. J., Alen, J., Ingham, T., Cryer, D. R., Stimpson, L. M., Ye, C.,
7 Seakins, P. W., Whalley, L. K., and Heard, D. E.: Implementation of a chemical background
8 method for atmospheric OH measurements by laser-induced fluorescence: characterisation
9 and observations from the UK and China, *Atmospheric Measurement Techniques*, 13, 3119–
10 3146, <https://doi.org/10.5194/amt-13-3119-2020>, 2020.

11 Xu, Z., Xue, L., Wang, T., Xia, T., Gao, Y., Louie, P. K. K., and Luk, C. W. Y.: Measurements of
12 Peroxyacetyl Nitrate at a Background Site in the Pearl River Delta Region: Production
13 Efficiency and Regional Transport, *Aerosol Air Qual. Res.*, 15, 833–841,
14 <https://doi.org/10.4209/aaqr.2014.11.0275>, 2015.

15 Yang, X., Lu, K., Ma, X., Liu, Y., Wang, H., Hu, R., Li, X., Lou, S., Chen, S., Dong, H., Wang, F.,
16 Wang, Y., Zhang, G., Li, S., Yang, S., Yang, Y., Kuang, C., Tan, Z., Chen, X., Qiu, P., Zeng, L., Xie,
17 P., and Zhang, Y.: Observations and modeling of OH and HO₂ radicals in Chengdu, China in
18 summer 2019, *Science of The Total Environment*, 772, 144829,
19 <https://doi.org/10.1016/j.scitotenv.2020.144829>, 2021.

20 Yang, X., Lu, K., Ma, X., Gao, Y., Tan, Z., Wang, H., Chen, X., Li, X., Huang, X., He, L., Tang, M.,
21 Zhu, B., Chen, S., Dong, H., Zeng, L., and Zhang, Y.: Radical chemistry in the Pearl River Delta:
22 observations and modeling of OH and HO₂ radicals in Shenzhen in 2018, *Atmospheric
Chemistry and Physics*, 22, 12525–12542, <https://doi.org/10.5194/acp-22-12525-2022>, 2022.

24 Yang, Y., Shao, M., Wang, X., Nölscher, A. C., Kessel, S., Guenther, A., and Williams, J.: Towards
25 a quantitative understanding of total OH reactivity: A review, *Atmospheric Environment*, 134,
26 147–161, <https://doi.org/10.1016/j.atmosenv.2016.03.010>, 2016.

27 Zou, Z., Chen, Q., Xia, M., Yuan, Q., Chen, Y., Wang, Y., Xiong, E., Wang, Z., and Wang, T.: OH
28 measurements in the coastal atmosphere of South China: possible missing OH sinks in aged
29 air masses, *Atmospheric Chemistry and Physics*, 23, 7057–7074, <https://doi.org/10.5194/acp-23-7057-2023>, 2023.

31

32

1 Supporting Information for

2 **Observation and modelling of OH and HO₂ radicals at a**
3 **subtropical rural site and implications for secondary**
4 **pollutants**

5 Zhouxing Zou^{1#}, Tianshu Chen^{1#}, Qianjie Chen¹, Weihang Sun¹, Shichun Han¹,
6 Zhuoyue Ren², Xinyi Li², Wei Song², Aoqi Ge², Qi Wang², Xiao Tian², Chenglei Pei³,
7 Xinming Wang², Yanli Zhang², and Tao Wang¹

8 [#] These authors contributed equally to this work

9 ¹ Department of Civil and Environmental Engineering, The Hong Kong Polytechnic
10 University, Hong Kong, China

11 ² Guangzhou Institute of Geochemistry, Chinese Academy of Sciences, Guangzhou,
12 China

13 ³ Guangdong Province Guangzhou Ecological Environment Monitoring Center
14 Station, Guangzhou 510030, China.

15 Correspondence to: Tao Wang (tao.wang@polyu.edu.hk)

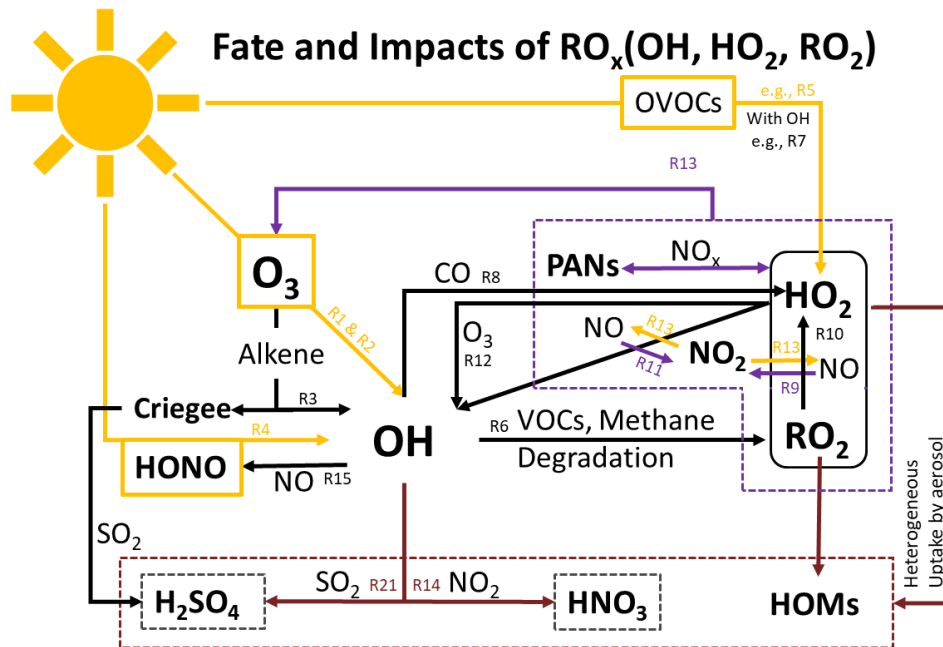
16 **Contents of this File**

17 20 pages

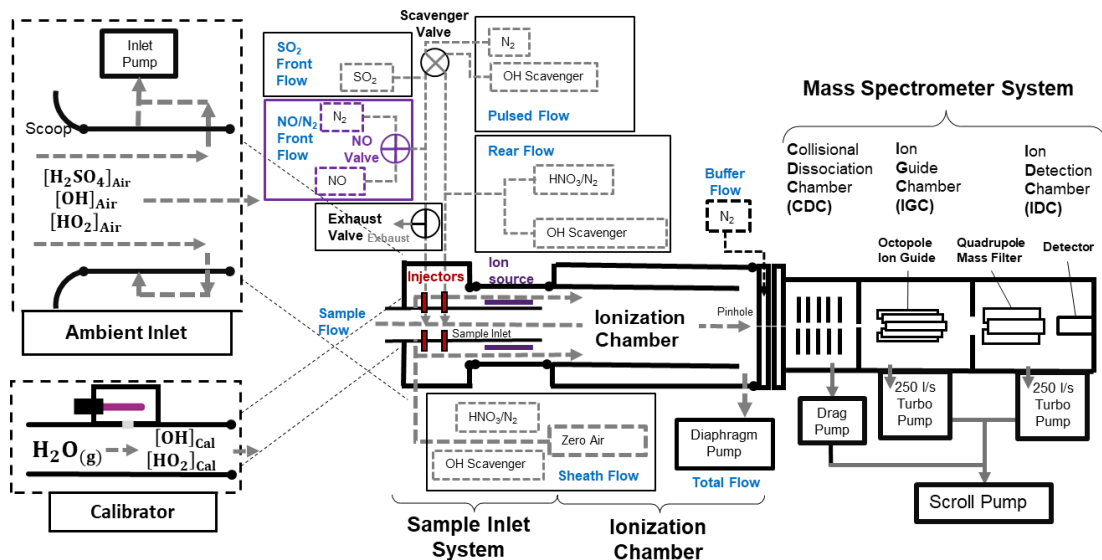
18 Figures: S1 to S7

19 Tables: S1 to S6

20 Text: S1 to S6

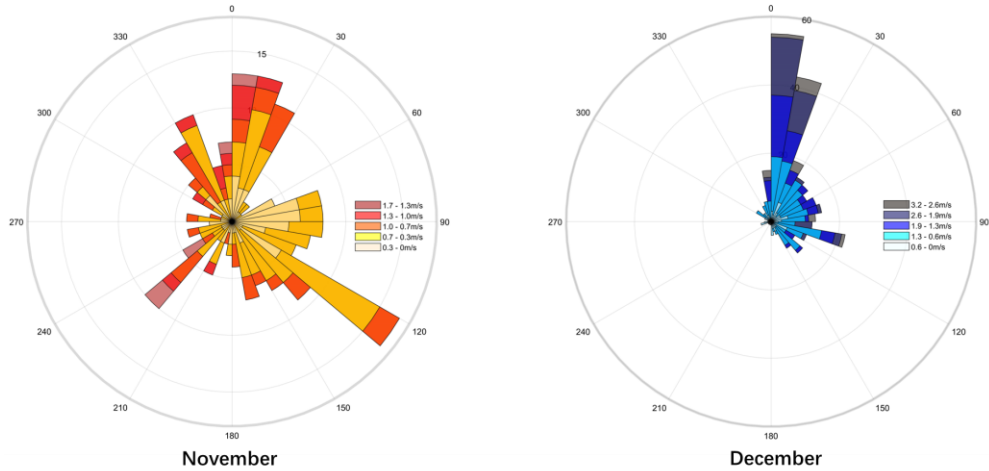


1 **Figure S1** Schematic of the RO_x family's photochemical pathway. Photolysis
2 reactions are highlighted in yellow, reactions contributing to secondary aerosol
3 production are marked in brown, and reactions associated with photochemical
4 pollution are indicated in purple. The chemical reactions (R1 to R21) referred to Table
5 S1.

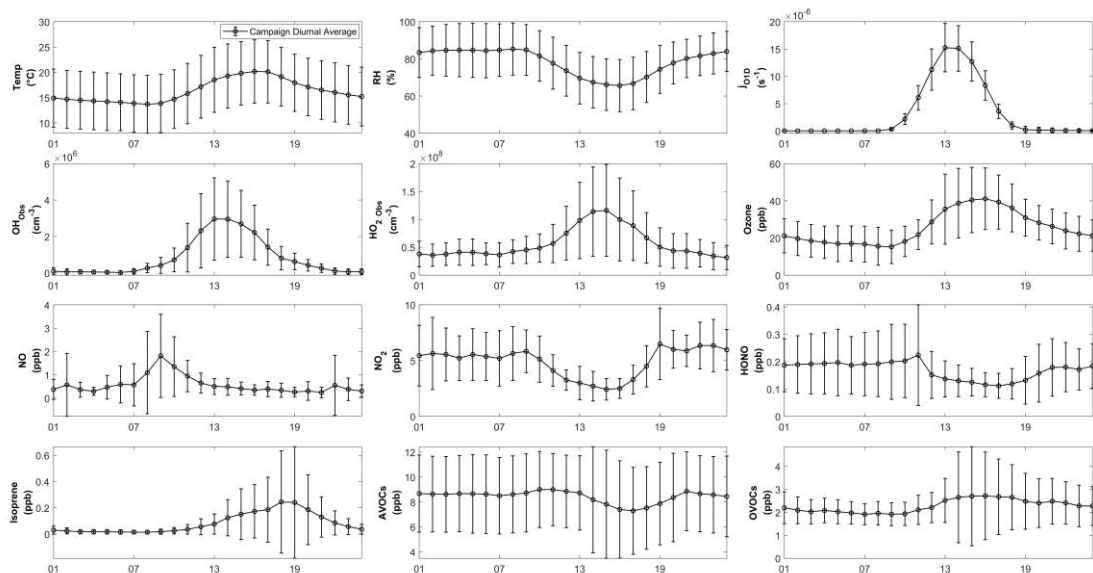


7 **Figure S2** Schematic diagram of the PolyU-CIMS system. The CIMS composed of
8 two detachable components: the ambient inlet and the calibrator; and the main body,
9 which includes the sample inlet system, ionization chamber, and the mass
10 spectrometer system. The frames labeled in purple highlight the additional valve
11 and flow paths.

1 incorporated for HO₂ measurement. Further details on setup, measurement principles
2 of the CIMS are available in a previous study in a previous study (Zou et al., 2023)
3 and Test S1.



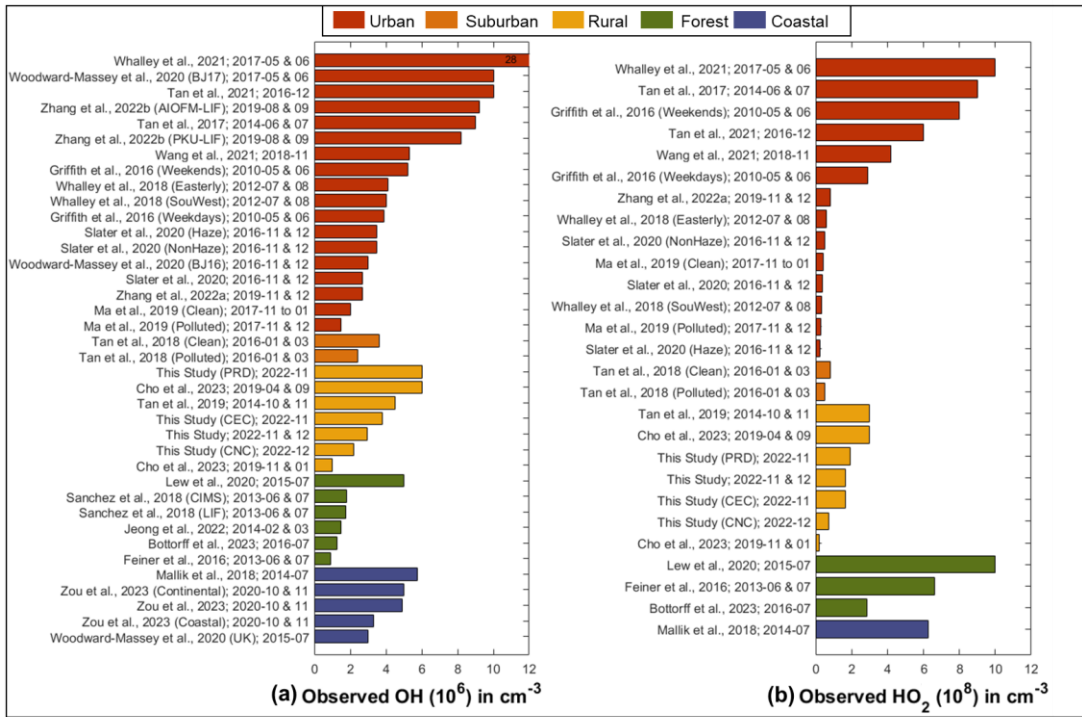
4
5 **Figure S3** The wind rose for November and December.



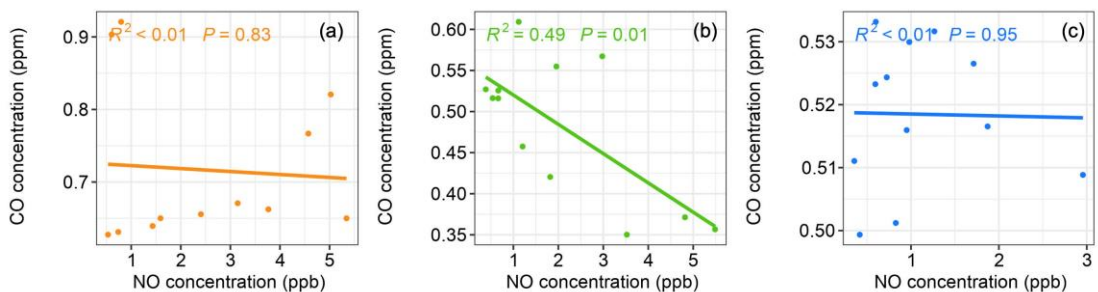
6
7 **Figure S4** Diurnal profiles of average concentration of HO₂, OH, meteorology data
8 and trace gases of the whole campaign. The shade error bars represent standard
9 deviations of the averaged data.

10

11



1
2 **Figure S5** Typical daily averaged maximum concentration of (a) OH and (b) HO₂
3 observed in various geophysical regions including coastal (blue), forest (green), rural
4 (yellow) and urban (red).



5
6 **Figure S6** Relationship between NO and CO concentrations in (a) PRD, (b) CEC and
7 (c) CNC from 7:00 to 10:00. The solid lines depict the linear regression fit, with the
8 corresponding equations R^2 and P values annotated on the plot.

9 **Table S1** The HO_x related reactions in the model.

Ambient: HO_x Productions	
(R1)	$O_3 + h\nu(<340 \text{ nm}) \rightarrow O(^1D) + O_2$
(R2)	$O(^1D) + H_2O \rightarrow OH + OH$
(R3)	$\text{Alkenes} + O_3 \rightarrow RO_X + \text{Products}$
(R4)	$\text{HONO} + h\nu(<400 \text{ nm}) \rightarrow OH + NO$
(R5)	$\text{HCHO} + h\nu (<335 \text{ nm}) + 2O_2 \rightarrow 2HO_2 + CO$
Ambient: HO_x Interconversions	
(R6)	$OH + RH + O_2 \rightarrow RO_2 + H_2O$
(R7)	$\text{HCHO} + OH + O_2 \rightarrow CO + H_2O + HO_2$
(R8)	$CO + OH + O_2 \rightarrow CO_2 + HO_2$
(R9)	$RO_2 + NO \rightarrow RO + NO_2$
(R10)	$RO + O_2 \rightarrow R'CHO + HO_2$
(R11)	$HO_2 + NO \rightarrow OH + NO_2$
(R12)	$HO_2 + O_3 \rightarrow OH + 2O_2$
(R13)	$NO_2 + h\nu(<420 \text{ nm}) + O_2 \rightarrow NO + O_3$
Ambient: HO_x Loss	
(R14)	$OH + NO_2 \rightarrow HNO_3$
(R15)	$OH + NO \rightarrow \text{HONO}$
(R16)	$RO_2 + NO \rightarrow RONO_2$
(R17)	$RO_2 + RO_2 \rightarrow \text{products}$
(R18)	$RO_2 + HO_2 \rightarrow ROOH + O_2$
(R19)	$HO_2 + HO_2 \rightarrow H_2O_2 + O_2$
(R20)	$HO_2 + HO_2 + H_2O \rightarrow H_2O_2 + H_2O + O_2$
(R21)	$OH + SO_2 + O_2 + H_2O + M \rightarrow H_2SO_4 + HO_2 + M$
CIMS: Reactions in Sample Inlet System	
(R21)	$OH + SO_2 + O_2 + H_2O + M \rightarrow H_2SO_4 + HO_2 + M$
(R11)	$HO_2 + NO \rightarrow OH + NO_2$
(R22)	$RO_2 + NO + O_2 \rightarrow R' CHO + HO_2 + NO_2$
(R23)	$\text{Scavenger gas} + OH \rightarrow \text{Products}$
CIMS: Reactions in Ionization Chamber	
(R24)	$HNO_3 + e^- \rightarrow NO_3^- + OH$
(R25)	$HNO_3 + NO_2^- \rightarrow NO_3^- + \text{HONO}$
(R26)	$NO_3^- + (HNO_3)_m + (H_2O)_n + M \rightarrow NO_3^- \cdot (HNO_3)_m \cdot (H_2O)_n + M$
(R27)	$H_2SO_4 + NO_3^- \cdot (HNO_3)_m \cdot (H_2O)_n \rightarrow HSO_4^- \cdot (HNO_3)_m \cdot (H_2O)_n + HNO_3$
CIMS: Reactions in Collisional Dissociation Chamber	
(R28)	$NO_3^- \cdot (HNO_3)_m \cdot (H_2O)_n + M \rightarrow NO_3^- + (HNO_3)_m + (H_2O)_n + M$
(R29)	$HSO_4^- \cdot (HNO_3)_m \cdot (H_2O)_n + M \rightarrow HSO_4^- + (HNO_3)_m + (H_2O)_n + M$
CIMS: Calibration	
(R30)	$H_2O + h\nu(184.9\text{nm}) + O_2 \rightarrow HO_2 + OH$

1

2

3 **Table S2** Summary of instruments used, and species measured during the field
4 campaign.

Instruments	Species	Resolution	Detection Limits	Accuracy
Q-CIMS (NO_3^-)	OH	1 hours	$3 \times 10^5 \text{ cm}^{-3}$	$\pm 46\%$
	HO_2	1 hours	$20 \times 10^5 \text{ cm}^{-3}$	$\pm 44\%$
Thermo 42i-TL	NO	1 min	60 ppt	$\pm 5.2\%$
Thermo 49i	O_3	1 min	0.5 ppb	$\pm 6.0\%$
NO ₂ -11r-EP	NO_2	1 min	60 ppt	$\pm 6.0\%$
Online GC-MS	VOCs	1 hour	10 ppt	$\pm 20\%$
Thermo 43i	SO_2	1 min	1 ppb	$\pm 6.1\%$
Thermo 48i	CO	1 min	40 ppb	$\pm 7.4\%$
Thermo 17i	NH_3	2 mins	1 ppb	$\pm 8\%$
LOPAP-03	HONO	5 mins	1 ppt	$\pm 10\%$
SMPS	Aerosol Particles	5 mins	$1 \text{ particle cm}^{-3}$	$\pm 10\%$

5

1 **Tabel S3** Configurations of the PolyU CIMS in Hok Tsui 2020 and Conghua 2022 campaigns. The changes from the last configuration were

a) Hok Tsui 2020								b) CongHua 2022							
Efficiency Related	Parameters	Gas	Values	Units	Specification for Measurement	Values	Units	Efficiency Related	Parameters	Gas	Values	Units	Specification for Measurement	Values	Units
E _{Conv}	Front Injection	SO ₂ (0.9%)	5	sccm	Sample Flow [SO ₂]	12	ppm	E _{conv}	Front Injection	SO ₂ (0.9%)	5	sccm	Sample Flow [SO ₂]	12	ppm
	Pulse Valve	N ₂ C ₃ F ₆ (99.9%)	2 2	sccm sccm	Cycle Duration (OH) B/S Ratio for OH measurement	6 8%	mins		Pulse Valve	N ₂ C ₃ F ₆ (99.9%)	2 2	sccm sccm	Cycle Duration (OH) Cycle Duration (HO ₂) B/S Ratio (OH) B/S Ratio (HO ₂)	6 60 10% 20%	mins
	Rear Injection	C ₃ F ₆ (99.9%) HNO ₃	2 10	sccm sccm	Sample Flow [C ₃ F ₆] Reaction Time	1072 47	ppm ms		Rear Injection	C ₃ F ₆ (99.9%) HNO ₃	2 10	sccm sccm	Sample Flow [C ₃ F ₆] Reaction Time	1072 47	ppm ms
	Sample Flow		3.7	slpm	Sample Flow Speed	55	cm/s		Sample Flow		3.7	slpm	Sample Flow Speed	55	cm/s
	Sheath Flow	Zero Air HNO ₃	12.6 10	slpm sccm	Reynolds Number in Ionization Chamber	>4000 Turbulent flows			Sheath Flow	Zero Air HNO ₃	12.6 10	slpm sccm	Reynolds Number in Ionization Chamber	>4000 Turbulent flows	
E _{Ion}		C ₃ F ₆ (99.9%)	2	sccm	Sheath Flow [C ₃ F ₆]	159	ppm	E _{Ion}		C ₃ F ₆ (99.9%)	2	sccm	Sheath Flow [C ₃ F ₆]	159	ppm
	Total Flow		16.8	slpm	Sheath Flow Speed	25	cm/s		Total Flow		16.8	slpm	Sheath Flow Speed	25	cm/s
	Sheath Voltages	-80 V			Voltages Difference	48	V		Sheath Voltages	-80 V			Voltages Difference	48	V
	Sample Voltages	-32 V			Voltages for ionization				Sample Voltages	-32 V			for ionization		
E _{Trans}	Buffer Gas	N ₂	440	sccm	Voltages Difference			E _{Trans}	Buffer Gas	N ₂	440	sccm	Voltages Difference		
	Buffer Voltages	-70 V			for transmission	80	V		Buffer Voltages	-70 V			for transmission	80	V
	Pinhole Voltages	-40 V							Pinhole Voltages	-40 V					
Cal	Calibration Flow	10	slpm		Calibration Factor			Cal	Calibration Flow	10	slpm		Calibration Factor	1.09*10 ⁻⁸	
	Flow Speed	65	cm/s		C _{OH}	1.21*10 ⁻⁸	cm ³		Flow Speed	65	cm/s		C _{HO2}	1.07*10 ⁻⁸	cm ³
	Product It Value	8.8*10 ¹⁰ photon/cm ²			(Reagent ion: N ¹⁸ O ₃ ⁻)				Product It Value	8.8*10 ¹⁰ photon/cm ²			(N ¹⁸ O ₃ ⁻) C _{H2SO4}	6.01*10 ⁻⁹	
Uncertainties	Sigma	2			Detection Limit	In lab	1.7	Uncertainties (2 σ)	Overall	OH	44%		Detection Limit in	OH	3
	Calibration	38%			($\times 10^5$ cm ³) (3 σ)	Day	12		H ₂ SO ₄	40%			Field Study	H ₂ SO ₄	1
	Overall	44%				Night	8.5		HO ₂	46%			($\times 10^5$ cm ³) (3 σ)	HO ₂	20

2 labelled by red color.

3 Notes: B/S Ratio - background to signal ratio

1 **Table S4** Average mixing ratios (ppbv) and standard deviations of measured VOCs
 2 that are constrained in the box model in the entire campaign and in different cases.

Species	Total	PRD	CEC	CNC	MCM Abb.
Ethane	2.3±0.83	1.6±0.88	1.9±0.53	2±0.14	C2H6
Ethylene	0.69±0.33	0.62±0.26	0.58±0.21	0.58±0.16	C2H4
Propane	1.6±0.62	2.1±0.81	1.2±0.31	1.2±0.27	C3H8
Propene	0.072±0.077	0.13±0.17	0.059±0.023	0.067±0.035	C3H6
i-Butane	0.44±0.28	0.89±0.49	0.35±0.1	0.31±0.061	IC4H10
n-Butane	0.65±0.41	1.3±0.71	0.48±0.14	0.44±0.083	NC4H10
Acetylene	0.92±0.42	0.91±0.35	0.82±0.31	0.76±0.072	C2H2
trans-2-Butene	0.015±0.0071	0.015±0.0046	0.017±0.011	0.016±0.0057	TBUT2ENE
cis-2-Butene	0.083±0.038	0.17±0.033	0.083±0.013	0.08±0.014	CBUT2ENE
Butene	0.044±0.021	0.047±0.049	0.037±0.014	0.048±0.01	BUT1ENE
Chloromethane	0.84±0.22	0.51±0.076	0.84±0.15	0.86±0.15	CH3CL
1,3-Butadiene	0.0079±0.0078	0.012±0.0087	0.0076±0.0071	0.007±0.0045	C4H6
Acetaldehyde	0.92±0.35	1.5±0.37	NaN	0.53±0.16	CH3CHO
Bromomethane	0.0093±0.0022	0.01±0.0019	0.009±0.0015	0.0088±0.00098	CH3BR
Chloroethane	0.023±0.012	0.015±0.011	0.021±0.0088	0.02±0.0039	CH3CH2CL
i-Pentane	0.34±0.17	0.61±0.22	0.31±0.059	0.24±0.042	IC5H12
1-Pentene	0.043±0.016	0.067±0.024	0.033±0.0079	0.037±0.0056	PENT1ENE
n-Pentane	0.19±0.1	0.34±0.18	0.12±0.034	0.14±0.022	NC5H12
trans-2-Pentene	0.0032±0.0045	0.011±0.0052	0.0025±0.0024	0.0012±0.0012	TPENT2ENE
Isoprene	0.082±0.17	0.26±0.34	0.16±0.2	0.029±0.03	C5H8
cis-2-Pentene	0.0017±0.0028	0.007±0.003	0.0012±0.0013	0.0039±0.0055	CPENT2ENE
Acrolein	0.06±0.031	0.092±0.043	0.053±0.019	0.043±0.015	ACR
Propanal	0.011±0.0059	0.015±0.011	0.0095±0.004	0.0091±0.0036	C2H5CHO
Vinylidene chloride	0.0036±0.0027	0.003±0.0016	0.002±0.002	0.0049±0.003	CCL2CH2
2,2-Dimethylbutane	0.017±0.015	0.046±0.025	0.012±0.0031	0.01±0.0015	M22C4
Dichloromethane	1.1±0.84	2.5±1.4	1±0.35	0.93±0.18	CH2CL2
2,3-Dimethylbutane	0.026±0.023	0.064±0.033	0.025±0.0066	0.015±0.004	M23C4
2-Methylpentane	0.071±0.045	0.24±0.053	0.06±0.016	0.056±0.012	M2PE
3-Methylpentane	0.052±0.039	0.12±0.061	0.04±0.011	0.036±0.0085	M3PE
Methyl tert-butyl ether	0.072±0.042	0.14±0.051	0.068±0.016	0.055±0.012	MTBE
1-Hexene	0.0048±0.0052	0.013±0.004	0.0036±0.004	0.002±0.0008	HEX1ENE
n-Hexane	0.066±0.043	0.13±0.063	0.049±0.016	0.042±0.012	NC6H14
Macrocyclic	0.062±0.062	0.12±0.058	0.11±0.069	0.025±0.0097	MACR
1,1-Dichloroethane	0.0086±0.0046	0.0079±0.0038	0.008±0.0036	0.0069±0.0014	CHCL2CH3
Butyraldehyde	0.54±0.21	0.45±0.18	0.5±0.14	0.45±0.16	C3H7CHO
1,2-Dichloroethylene	0.049±0.076	0.14±0.17	0.032±0.014	0.026±0.014	DICLETH
2-Butanone	0.25±0.24	0.55±0.49	0.21±0.086	0.13±0.05	MEK
Ethyl acetate	0.27±0.39	0.71±0.87	0.17±0.076	0.15±0.076	ETHACET
Chloroform	0.082±0.032	0.13±0.042	0.087±0.015	0.069±0.01	CHCL3
Methylchloroform	0.0021±0.0011	0.0037±0.00044	0.001±4.4e-19	0.0018±0.00042	CH3CCL3
2-Methylhexane	0.015±0.017	0.046±0.028	0.0097±0.0038	0.0074±0.002	M2HEX
Cyclohexane	0.019±0.015	0.041±0.021	0.011±0.0052	0.011±0.0037	CHEX
Tetrachloromethane	0.073±0.0055	0.07±0.0036	0.066±0.0036	0.075±0.0031	CCL4
3-Methylhexane	0.02±0.024	0.064±0.042	0.012±0.0042	0.0095±0.0026	M3HEX
Benzene	0.35±0.14	0.29±0.11	0.32±0.1	0.31±0.029	BENZENE
Ethylene dichloride	0.36±0.17	0.26±0.11	0.34±0.18	0.41±0.097	CH2CLCH2Cl
n-Hepane	0.035±0.023	0.072±0.038	0.024±0.0053	0.022±0.0035	NC7H16
Crotonaldehyde	0.45±0.14	0.46±0.079	0.48±0.065	0.5±0.0081	C3MDBAL
Trichloroethene	0.021±0.023	0.061±0.037	0.018±0.013	0.013±0.0033	TRICLETH
1,2-Dichloropropane	0.085±0.038	0.12±0.03	0.096±0.016	0.071±0.011	CL12PROP
Pantanal	0.018±0.011	0.033±0.017	0.019±0.0078	0.013±0.006	C4H9CHO
1,3-Dichloro-1-propene	0.0025±0.0011	0.0029±0.00071	0.0015±0.00099	0.0024±0.00092	CLC3H4CL
4-Methyl-2-pentanone	0.0046±0.0073	0.019±0.0045	0.0011±0.00091	0.0031±0.0051	MIBK
Toluene	0.28±0.27	0.71±0.5	0.21±0.057	0.17±0.049	TOLUENE
n-Octane	0.0093±0.0071	0.022±0.0067	0.0046±0.0014	0.0051±0.0012	NC8H18
1,1,2-Trichloroethane	0.014±0.0097	0.011±0.0084	0.013±0.0093	0.015±0.0048	CH2CLCHCl2
Tetrachloroethylene	0.015±0.013	0.04±0.019	0.014±0.004	0.0085±0.0011	TCE
2-Hexanone	0.05±0.025	0.087±0.029	NaN	0.038±0.011	HEX2ONE
Hexanal	0.041±0.022	0.076±0.025	NaN	0.03±0.0091	C5H11CHO
1,2-Dibromoethane	0.002±0.0016	0.0038±0.0012	0.0013±0.0012	0.0015±0.0011	DIBRET
Ethylbenzene	0.042±0.031	0.072±0.035	0.028±0.022	0.034±0.023	EBENZ
o-Xylene	0.039±0.03	0.077±0.039	0.027±0.018	0.031±0.017	OXYL
Styrene	0.02±0.013	0.034±0.008	0.012±0.0054	0.013±0.0074	STYRENE
Isopropylbenzene	0.006±0.0058	0.016±0.0026	0.0027±0.0011	0.0029±0.00099	IPBENZ
1,1,2,2-Tetrachloroethane	0.0031±0.0019	0.0053±0.0012	0.0029±0.0017	0.0023±0.0012	CHCL2CHCl2
n-Propylbenzene	0.0048±0.0045	0.013±0.0033	0.0032±0.0013	0.0024±0.001	PBENZ
m-Ethyltoluene	0.0073±0.0067	0.019±0.0083	0.0057±0.0026	0.0041±0.0018	METHTOL
p-Ethyltoluene	0.0048±0.0047	0.013±0.0045	0.0033±0.002	0.0024±0.0015	PETHTOL
1,3,5-Trimethylbenzene	0.0051±0.0054	0.015±0.0054	0.004±0.0022	0.0021±0.0015	TM135B
n-Decane	0.0031±0.0031	0.0088±0.0028	0.0017±0.00075	0.0013±0.00062	NC10H22
Benzaldehyde	0.0047±0.0044	0.013±0.0039	0.0032±0.0013	0.0023±0.00098	BENZAL
1,2,4-Trimethylbenzene	0.0088±0.009	0.024±0.013	0.0075±0.0031	0.0044±0.0019	TM124B
1,2,3-Trimethylbenzene	0.0037±0.0035	0.01±0.0037	0.0029±0.0015	0.0018±0.001	TM123B
Undecane	0.0019±0.0024	0.0061±0.0012	0.0018±0.00091	0.0037±0.0056	NC11H24
Dodecane	0.0094±0.0035	0.015±0.0034	0.0066±0.0014	0.01±0.0017	NC12H26

1 **Text S1 Calibration procedures**

2 The calibration of Chemical Ionization Mass Spectrometer (CIMS) involves the
3 generation of OH and HO₂ radicals through photolysis of water vapor by 184.9 nm
4 light, as outlined in Reaction R30. The concentration of radicals produced during
5 calibration is determined from the known concentration of water vapor [H₂O], which
6 is calculated from water vapor pressure and the relative humidity and temperature.
7 Other essential parameters include the photolysis cross-section of water vapor ($\sigma_{H_2O} =$
8 $7.14 \times 10^{-20} \text{ cm}^2$; Cantrell et al., 1997), the photolysis quantum yield (Φ , assumed to
9 be 1, Kürten et al., 2012) and the photon flux (It value, see details about It value
10 determination on Kürten et al., 2012). The generated radical concentrations ([OH] and
11 [HO₂]) are calculated using the following equations:

12
$$[OH] = [HO_2] = [H_2O] * \sigma_{H_2O} * \Phi * It$$

13 From these values, the calibration factors for OH and HO₂ (C_{OH} and C_{HO_2}) are
14 calculated using the signals obtained during calibration (S_{OHcal} and S_{HO2cal}), as
15 expressed in the transformed equations E1 and E2:

16
$$C_{OH} = \frac{1}{[OH]_{cal}} \times \frac{S_{OHcal}}{S_{62}} \text{ (E1, transformed)}$$

17
$$C_{HO_2} = \frac{1}{[HO_2]_{cal}} \times \frac{S_{HO2cal}}{S_{62}} \text{ (E2, transformed)}$$

18 The calibrator produced OH and HO₂ concentrations in the range of 3×10^7 to 1×10^9
19 cm⁻³ depending on RH conditions in 10 LMP synthetic air. The more detailed
20 information on calculation procedures is given in our previous study (Zou et al.,
21 2023).

22 **Text S2 Modification for HO₂ measurement**

23 To measure the HO₂, a valve is added to switch the injection gas between NO and
24 N₂ as indicated by purple frame in Figure S2. When adding N₂, the CIMS is in OH
25 measurement mode. When NO is added to the sample flow, the CIMS changes to HO₂
26 mode for total HO_x measurement.

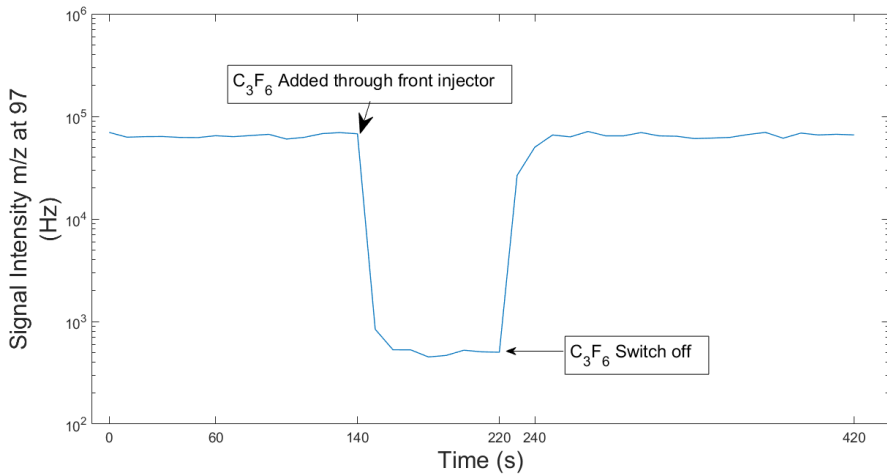
27 During HO₂ measurement, ambient HO₂ converted by NO to OH. It should be
28 noted that in HO₂ mode, the increasing NO concentration can enhance HO₂

1 conversion to OH (R11), but excessive NO levels trigger the HONO formation when
2 reacts with OH (R15), competing with the OH conversion process by SO₂ (R21) and
3 lowering the detection efficiency for OH. Consequently, the NO to SO₂ concentration
4 ratio is crucial for HO₂ measurements. Sensitivity tests revealed an optimal
5 [NO]/[SO₂] ratio of 0.1 for the PolyU-CIMS and 100% conversion of HO₂ in the
6 laboratory ([H₂SO₄]/[HO₂] = 1), aligning with prior research recommendations
7 (Edwards et al., 2003; Sjostedt et al., 2007). Because the concentrations of both SO₂
8 and NO injected to sample flow are maintained at levels over 100-1000 times higher
9 than those in the ambient atmosphere and the injection flow rates are fixed, the
10 efficiency of the HO₂ to OH conversion remains stable and is believed to be at
11 completion.

12 Text S3 The Background mode and scavenge efficiency

13 In the background mode, scavenger gases C₃F₆ are introduced into the sample
14 flow along with SO₂. Given that the concentration of C₃F₆ is 100 times higher than
15 that of SO₂, the ambient OH and any ambient HO₂ converted to OH are scavenged by
16 C₃F₆, rather than being converted to H₂SO₄.

17 To determine the amount of C₃F₆ that is needed to achieve complete OH
18 scavenge, we gradually increased C₃F₆ added to high concentrations of OH and HO₂
19 ([HO_x] \approx 10⁹ cm⁻³) generated from the calibrator in synthetic air until no further
20 reduction in the measured signal, which indicates complete scavenging of OH. This
21 point defines the background noise which is attributed to any Criegee intermediates
22 and ambient sulfuric acid. In our setup, there is residual C₃F₆ present after CIMS
23 switches from background to signal mode, but it does not affect the measurement
24 results. As shown in Figure S7, after switching off C₃F₆, the measurement signals
25 rapidly return to their initial levels within 20 seconds. Data affected by C₃F₆ residual
26 are excluded to minimize the impact of the residual C₃F₆ on the measurements.



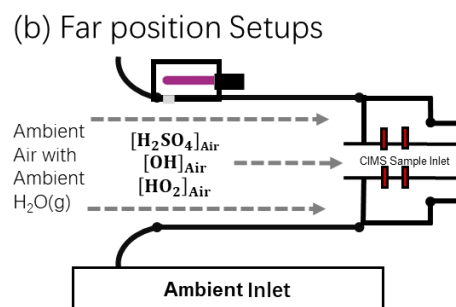
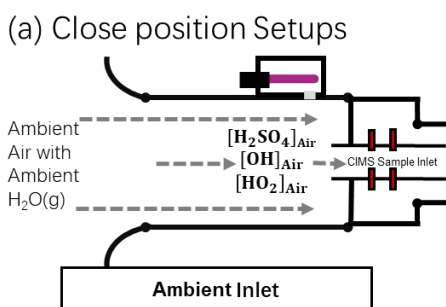
1

2 **Figure S7** Variation of signal intensity m/z at 97 before C_3F_6 addition with time, after
 3 addition and switching off of C_3F_6 in synthetic air containing OH of $\sim 5 \times 10^8 \text{ cm}^{-3}$.

4 **Text S4 Measurement interferences**

5 **4.1 Sampling Loss**

6 Wall losses in the ambient inlet were evaluated by varying the distances of the
 7 calibration lamp from the inlet to assess potential effects on signal attenuation. The
 8 instrument was calibrated in two distinct configurations: initially, the lamp was
 9 positioned close to the CIMS sample inlet (Figure S6a, and subsequently, moved
 10 away from the CIMS sample inlet (Figure S6b. By comparing the observed signals
 11 from these two configurations, we were able to calculate the wall losses associated
 12 with the ambient inlet. The results indicated no significant difference (<1%) between
 13 the two measurements, suggesting negligible wall losses in the sampling system.



14

15 **Figure S8** calibration process during ambient sampling in (a) close and (b) far
 16 positions.

1 Furthermore, the potential for radical-radical loss after radicals exit the calibrator
2 and enter the sampling inlet was considered. Given the flow speed of the ambient inlet
3 (12.2 m/s), the sample inlet (55 cm/s), and the distances involved—the calibration
4 lamp is less than 1 cm from the sample inlet, and the sampling port to the front
5 injectors is 1 cm—it can be calculated that the transport time for radicals to the front
6 injectors for reactions is less than 20 ms. This brief transport time is sufficiently short
7 to prevent significant radical-radical losses. Additionally, since the sample inlet draws
8 the central part of the airflow within the ambient inlet, and the flow in the sample inlet
9 is laminar, wall losses at this stage are also considered negligible.

10 **4.2 OH interference**

11 The OH interference in PolyU-CIMS, resulting from ambient HO₂ recycling
12 (R11) and ionization process (R24, artificial OH), was accounted for and included in
13 the measurement uncertainty, as outlined by Zou et al. (2023). However, in this study,
14 PolyU-CIMS encountered additional interference from residual NO in the injectors
15 when switching from NO (used for HO₂ measurement) to N₂ (used for OH
16 measurement). To prevent residual NO buildup, the inlet was cleaned daily, and a
17 one-hour calibration was performed at both the start and end of daily measurement to
18 monitor the NO residuals. The monitoring results showed that the NO residual time
19 for PolyU - CIMS was approximately 26 mins which is similar to the residual time
20 reported in earlier studies (Edwards et al., 2003; Sjostedt et al., 2007). Consequently,
21 data collected during the residual period (30 mins after switching the measurement
22 target from HO₂ to OH) was discarded to eliminate any NO residual interference from
23 the final results. See details about how the duty cycle setup achieved the monitoring
24 of NO residual interference in Text S5.

25 **4.3 HO₂ interference**

26 The concentration of injected NO is the primary source of HO₂ measurement
27 interference in this study. High NO concentrations convert ambient RO₂, particularly
28 alkene and aromatic-related RO₂, into HO₂ and then OH, leading to a positive bias in
29 HO₂ measurements (Fuchs et al., 2014). To mitigate this interference, the NO

1 concentration at the sample inlet was set to 1.2 ppm—lower than the levels
2 recommended in previous studies to minimize RO₂ interference (Fuchs et al., 2014).

3 To assess the possible HO₂ interference from RO₂, we first simulated with a box
4 model production of HO₂ from RO₂ in the inlet system with addition of 1.2 ppm NO
5 to ambient air composition observed in previous field study in Hok Tsui (a coastal site
6 in Hong Kong) by our team in 2020 (Zou et al., 2023) before this observation. The
7 observation-constrained MCM model (described in the Text S6) was run for three
8 days, and the RO₂ outputs were taken as used as the initial concentrations entering the
9 inlet. Then another model run was conducted by setting j-values setting to zero and
10 reaction time as the residence time (47 ms) to simulate the conversion of RO₂ by NO
11 in the CIMS inlet. We compared the OH concentrations (from RO₂ conversion to HO₂
12 and then to OH) at the outlet with the total concentration of HO₂+OH after spinning
13 up. The result shows a difference of less than 2% suggesting negligible conversation
14 of RO₂ to HO₂ in the inlet at 1.2 ppm NO injection. Similar model tests with real time
15 conditions were also done for Conghua study after field study and show less than 2%
16 interference.

17 To verify the model results, experiment tests were conducted in both laboratory
18 and field settings (Hok Tsui in Hong Kong and Conghua) by comparing the HO₂
19 calibration factor obtained in synthetic air (with minimal interference of RO₂ due to
20 very low VOCs concentrations in the synthetic air) and that conducted in indoor and
21 outdoor air (with potential interference due to presence of VOCs). The results in
22 Table S6 show difference of 1% - 3% between the HO₂ calibration factor in the
23 synthetic air with that in the lab indoor air and that in the ambient air at Hok Tsui
24 (with [O₃] <70 ppb [NO_x] < 10 ppb) as well as Cong Hua (with [O₃] <60 ppb [NO_x] <
25 10 ppb), confirming little interference of RO₂ to HO₂ measurements (See Table S6
26 below). These results might be due to the low concentrations of biogenic volatile
27 organic compounds (BVOCs) in our two study sites ([C₅H₈] <0.2 ppb) as previous
28 studies show large interference of BVOC than anthropogenic VOC to HO₂
29 measurements (Fuchs et al., 2014).

30 **Table S5**Calibration factors of OH and HO₂ obtained in different conditions to
31 estimate the RO₂ interference.

Year of experiments	Calibration Conditions	Calibration Factor (cm ³)		Notes
		OH	HO ₂	
2021	Synthetic air in lab	7.912E-10	9.156E-10	On the afternoon of
	Indoor air in lab	8.146E-10	9.275E-10	<u>Nov 20, 2021</u>
	Synthetic air at Hok Tsui	8.212E-10	9.181E-10	On the morning of
	Outdoor air at Hok Tsui	8.252E-10	9.378E-10	Dec 23, 2021
2022	Synthetic air in lab	1.043E-09	1.080E-09	On the morning of
	Indoor air in lab	1.035E-09	1.119E-09	<u>May 04, 2022</u>
	Synthetic air at Conghua	1.033E-09	1.085E-09	On the morning of
	Outdoor air at Conghua	1.025E-09	1.092E-09	Nov 17, 2022

Notes:

The difference between calibration factors obtained at 2022 and 2020 is due to the changes of CIMS's settings

Chemical Condition of outdoor air of Hok Tsui [O₃] <70 ppb, [NO_x] < 10 ppb, [C₅H₈] < 0.2 ppb

Chemical Condition of outdoor air of Cong Hua [O₃] <60 ppb, [NO_x] < 10 ppb, C₅H₈] < 0.2 ppb

1

2 Text S5 The measurement duty cycle of CIMS

3 As detailed in Section 2.2, the PolyU-CIMS was configured to sequentially
 4 measure HO₂, H₂SO₄, and OH within each hour during the field study, corresponding
 5 to changes in injection gases. Table S3 outlines the hourly schedule and injection
 6 gases Figure S9 a 1-hour duty cycle.

7 Table S6 Duty cycle and injection gases for targeted chemical analysis.

Purpose	Measure ment Mode	Signal 97 Label	Chemicals injected to the sample flow through different injectors		Duty time (s)	Repeat times	Total Duration (mins)
			Front Injectors	Rear Injectors			
HO ₂	SIG	S ₉₇ NO	NO, N _{2(p)} , SO ₂ ,	Sca, Sca _(p)	60	3	6
	BKG	S ₉₇ NOsca	NO, Sca _(p) , SO ₂	Sca, N _{2(p)}	60		
H ₂ SO ₄	SIG	S ₉₇ w/o	-	Sca, Sca _(p)	60	2	4
	BKG	S ₉₇ w/o	-	Sca, N _{2(p)}	60		
OH	SIG	S ₉₇ SO ₂	N _{2(p)} , SO ₂ ,	Sca, Sca _(p)	60	25	50
	BKG	S ₉₇ SO ₂ sca	Sca _(p) , SO ₂	Sca, N _{2(p)}	60		

8

Notes:

Front and Rear Injectors - The injector pairs as demonstrated in the

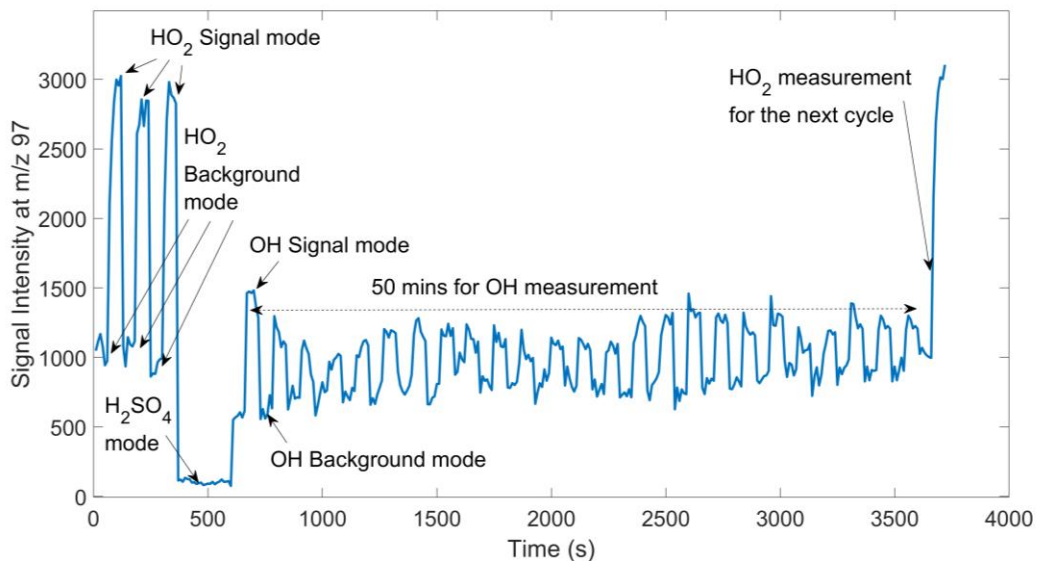
Figure S2

SIG & BKG – the signal and background modes.

Sca - scavenger gas, C₃F₆ in this study.

Sca_(p) - scavenger gas added through the pulsed flow.

N_{2(p)} - nitrogen gas, added through the pulsed flow.



1

2 Figure S9 Variation of signal intensity at m/z 97 during a 1-hour duty cycle of CIMS
 3 measurement.

4 **Text S6 The model efforts to correct measurement interference.**

5 Ambient NO can cause interference to OH measurement by converting HO₂ to
 6 OH in the inlet system. To assess and correct this effect, model simulations were
 7 conducted, which also simulated conversion of RO₂ to HO₂ by NO (i.e., interference
 8 to HO₂ measurements as discussed before). We first constrained all measured species
 9 (except OH and HO₂) in the model, and a three-day spin-up was used to simulate the
 10 chemical conditions of the sampled air during measurement. Then the outputs were
 11 used as inputs for another simulation with the injection gases (SO₂ and/or NO) to
 12 simulate chemical reactions in the inlet with reaction time of 47 ms to match the
 13 reaction time in the CIMS. Photolysis frequencies were maintained at zero to reflect
 14 the dark environment of the inlet. The modeled OH concentrations without NO
 15 addition and OH concentrations with NO addition represent ambient NO interference
 16 to OH and HO₂, respectively.

17 The calculated interferences for OH and HO₂ measurements were in the range
 18 1×10⁴ cm⁻³ to 1×10⁵ cm⁻³ (mean: 3×10⁴) and 8×10⁵ cm⁻³ to 2×10⁶ cm⁻³ (mean:
 19 1.2×10⁶), respectively. These lead to correction of measurement data of OH and HO₂
 20 less than 2%.

1 **Text S7: Sensitivity Test to assess impact of the fresh vehicle exhaust in CEC**

2 A sensitivity test was conducted for the CEC case to account for the missing OH
3 reactivity in the morning. This missing OH reactivity was attributed to unmeasured
4 species in the fresh diesel exhaust. To estimate this, we first calculated the total OH
5 reactivity of the exhaust based on the reactivity of NO_x and CO, along with the diesel
6 exhaust source profile. The contributions from NO_x and CO were then subtracted. The
7 remaining OH reactivity was allocated to formaldehyde and acetaldehyde, with their
8 concentrations adjusted accordingly. This allocation was justified by the significant
9 contribution of OVOCs to the total reactivity of diesel exhaust (Yao et al., 2015; Mo
10 et al., 2016), as formaldehyde and acetaldehyde were not measured in this study. The
11 sensitivity test was performed following these steps:

12 1. First, we calculated the OH reactivity of freshly emitted NO_x and CO at each
13 time step. We assumed that the pollutant concentrations at the time of the highest NO
14 concentration did not undergo significant photochemical loss. For each time step, we
15 calculated the ratio of the OH concentration at the time of the highest NO
16 concentration to the OH concentration at that time step. This ratio was then multiplied
17 by the OH reactivity of ambient NO_x and CO at that time step to estimate the OH
18 reactivity from the emitted NO_x and CO.

19 2. The observed exhaust OH reactivity was determined by dividing the OH
20 reactivity of emitted NO_x and CO by 20%, which represents the minimum
21 contribution of NO_x and CO to the observed OH reactivity in exhaust in China (Yang,
22 2023).

23 3. The total exhaust OH reactivity was derived by dividing the observed exhaust
24 OH reactivity by 60%, to account for the approximately 40% of OH reactivity missing
25 in Chinese diesel exhaust (Yang, 2023). The OH reactivity of emitted NO_x and CO
26 was then subtracted from the total exhaust OH reactivity.

27 4. The remaining OH reactivity was allocated to formaldehyde and acetaldehyde
28 in a 1:1.6 ratio, and their concentrations were adjusted accordingly. This ratio was

1 calculated based on the concentration ratios of formaldehyde and acetaldehyde in
2 diesel exhaust (Yao et al., 2015) and their respective OH reactivity coefficients.

3 **Reference**

4 Bottorff, B., Lew, M. M., Woo, Y., Rickly, P., Rollings, M. D., Deming, B., Anderson,
5 D. C., Wood, E., Alwe, H. D., Millet, D. B., Weinheimer, A., Tyndall, G., Ortega, J.,
6 Dusanter, S., Leonardi, T., Flynn, J., Erickson, M., Alvarez, S., Rivera-Rios, J. C.,
7 Shutter, J. D., Keutsch, F., Helmig, D., Wang, W., Allen, H. M., Slade, J. H., Shepson,
8 P. B., Bertman, S., and Stevens, P. S.: OH, HO₂, and RO₂ radical chemistry in a rural
9 forest environment: measurements, model comparisons, and evidence of a missing
10 radical sink, *Atmospheric Chemistry and Physics*, 23, 10287–10311,
11 <https://doi.org/10.5194/acp-23-10287-2023>, 2023.

12 Cho, C., Fuchs, H., Hofzumahaus, A., Holland, F., Bloss, W. J., Bohn, B., Dorn, H.-P.,
13 Glowania, M., Hohaus, T., Liu, L., Monks, P. S., Niether, D., Rohrer, F., Sommariva,
14 R., Tan, Z., Tillmann, R., Kiendler-Scharr, A., Wahner, A., and Novelli, A.:
15 Experimental chemical budgets of OH, HO₂, and RO₂ radicals in rural air in western
16 Germany during the JULIAC campaign 2019, *Atmospheric Chemistry and Physics*, 23,
17 2003–2033, <https://doi.org/10.5194/acp-23-2003-2023>, 2023.

18 Edwards, G. D., Cantrell, C. A., Stephens, S., Hill, B., Goyea, O., Shetter, R. E.,
19 Mauldin, R. L., Kosciuch, E., Tanner, D. J., and Eisele, F. L.: Chemical Ionization Mass
20 Spectrometer Instrument for the Measurement of Tropospheric HO₂ and RO₂, *Anal.
Chem.*, 75, 5317–5327, <https://doi.org/10.1021/ac034402b>, 2003.

22 Feiner, P. A., Brune, W. H., Miller, D. O., Zhang, L., Cohen, R. C., Romer, P. S.,
23 Goldstein, A. H., Keutsch, F. N., Skog, K. M., Wennberg, P. O., Nguyen, T. B., Teng,
24 A. P., DeGouw, J., Koss, A., Wild, R. J., Brown, S. S., Guenther, A., Edgerton, E.,
25 Baumann, K., and Fry, J. L.: Testing Atmospheric Oxidation in an Alabama Forest,
26 *Journal of the Atmospheric Sciences*, 73, 4699–4710, <https://doi.org/10.1175/JAS-D-16-0044.1>, 2016.

1 Fuchs, H., Acir, I.-H., Bohn, B., Brauers, T., Dorn, H.-P., Häseler, R., Hofzumahaus, A.,
2 Holland, F., Kaminski, M., Li, X., Lu, K., Lutz, A., Nehr, S., Rohrer, F., Tillmann, R.,
3 Wegener, R., and Wahner, A.: OH regeneration from methacrolein oxidation
4 investigated in the atmosphere simulation chamber SAPHIR, *Atmos. Chem. Phys.*, 14,
5 7895–7908, <https://doi.org/10.5194/acp-14-7895-2014>, 2014.

6 Griffith, S. M., Hansen, R. F., Dusanter, S., Michoud, V., Gilman, J. B., Kuster, W. C.,
7 Veres, P. R., Graus, M., Gouw, J. A., Roberts, J., Young, C., Washenfelder, R., Brown,
8 S. S., Thalman, R., Waxman, E., Volkamer, R., Tsai, C., Stutz, J., Flynn, J. H., Grossberg,
9 N., Lefer, B., Alvarez, S. L., Rappenglueck, B., Mielke, L. H., Osthoff, H. D., and
10 Stevens, P. S.: Measurements of hydroxyl and hydroperoxy radicals during CalNex-LA:
11 Model comparisons and radical budgets, *J. Geophys. Res. Atmos.*, 121, 4211–4232,
12 <https://doi.org/10.1002/2015JD024358>, 2016.

13 Jeong, D., Seco, R., Emmons, L., Schwantes, R., Liu, Y., McKinney, K. A., Martin, S.
14 T., Keutsch, F. N., Gu, D., Guenther, A. B., Vega, O., Tota, J., Souza, R. A. F.,
15 Springston, S. R., Watson, T. B., and Kim, S.: Reconciling Observed and Predicted
16 Tropical Rainforest OH Concentrations, *JGR Atmospheres*, 127,
17 <https://doi.org/10.1029/2020JD032901>, 2022.

18 Lew, M. M., Rickly, P. S., Bottorff, B. P., Reidy, E., Sklaveniti, S., Léonardis, T., Locoge,
19 N., Dusanter, S., Kundu, S., Wood, E., and Stevens, P. S.: OH and HO₂ radical chemistry
20 in a midlatitude forest: measurements and model comparisons, *Atmospheric Chemistry
and Physics*, 20, 9209–9230, <https://doi.org/10.5194/acp-20-9209-2020>, 2020.

22 Ma, X., Tan, Z., Lu, K., Yang, X., Liu, Y., Li, S., Li, X., Chen, S., Novelli, A., Cho, C.,
23 Zeng, L., Wahner, A., and Zhang, Y.: Winter photochemistry in Beijing: Observation
24 and model simulation of OH and HO₂ radicals at an urban site, *Science of The Total
25 Environment*, 685, 85–95, <https://doi.org/10.1016/j.scitotenv.2019.05.329>, 2019.

26 Mallik, C., Tomsche, L., Bourtsoukidis, E., Crowley, J. N., Derstroff, B., Fischer, H.,
27 Hafermann, S., Hüser, I., Javed, U., Keßel, S., Lelieveld, J., Martinez, M., Meusel, H.,
28 Novelli, A., Phillips, G. J., Pozzer, A., Reiffs, A., Sander, R., Taraborrelli, D., Sauvage,

1 C., Schuladen, J., Su, H., Williams, J., and Harder, H.: Oxidation processes in the
2 eastern Mediterranean atmosphere: evidence from the modelling of HO_x measurements
3 over Cyprus, *Atmospheric Chemistry and Physics*, 18, 10825–10847,
4 <https://doi.org/10.5194/acp-18-10825-2018>, 2018.

5 Mo, Z., Shao, M., and Lu, S.: Compilation of a source profile database for hydrocarbon
6 and OVOC emissions in China, *Atmos. Environ.*, 143, 209–217,
7 <https://doi.org/10.1016/j.atmosenv.2016.08.025>, 2016.

8 Sanchez, D., Jeong, D., Seco, R., Wrangham, I., Park, J.-H., Brune, W. H., Koss, A.,
9 Gilman, J., de Gouw, J., Misztal, P., Goldstein, A., Baumann, K., Wennberg, P. O.,
10 Keutsch, F. N., Guenther, A., and Kim, S.: Intercomparison of OH and OH reactivity
11 measurements in a high isoprene and low NO environment during the Southern Oxidant
12 and Aerosol Study (SOAS), *Atmospheric Environment*, 174, 227–236,
13 <https://doi.org/10.1016/j.atmosenv.2017.10.056>, 2018.

14 Sjostedt, S. J., Huey, L. G., Tanner, D. J., Peischl, J., Chen, G., Dibb, J. E., Lefer, B.,
15 Hutterli, M. A., Beyersdorf, A. J., Blake, N. J., Blake, D. R., Sueper, D., Ryerson, T.,
16 Burkhardt, J., and Stohl, A.: Observations of hydroxyl and the sum of peroxy radicals at
17 Summit, Greenland during summer 2003, *Atmospheric Environment*, 41, 5122–5137,
18 <https://doi.org/10.1016/j.atmosenv.2006.06.065>, 2007.

19 Slater, E. J., Whalley, L. K., Woodward-Massey, R., Ye, C., Lee, J. D., Squires, F.,
20 Hopkins, J. R., Dunmore, R. E., Shaw, M., Hamilton, J. F., Lewis, A. C., Crilley, L. R.,
21 Kramer, L., Bloss, W., Vu, T., Sun, Y., Xu, W., Yue, S., Ren, L., Acton, W. J. F., Hewitt,
22 C. N., Wang, X., Fu, P., and Heard, D. E.: Elevated levels of OH observed in haze events
23 during wintertime in central Beijing, *Atmospheric Chemistry and Physics*, 20, 14847–
24 14871, <https://doi.org/10.5194/acp-20-14847-2020>, 2020.

25 Tan, Z., Fuchs, H., Lu, K., Hofzumahaus, A., Bohn, B., Broch, S., Dong, H., Gomm, S.,
26 Häseler, R., He, L., Holland, F., Li, X., Liu, Y., Lu, S., Rohrer, F., Shao, M., Wang, B.,
27 Wang, M., Wu, Y., Zeng, L., Zhang, Y., Wahner, A., and Zhang, Y.: Radical chemistry

1 at a rural site (Wangdu) in the North China Plain: observation and model calculations
2 of OH, HO₂ and RO₂ radicals, *Atmospheric Chemistry and Physics*, 17, 663–690,
3 <https://doi.org/10.5194/acp-17-663-2017>, 2017.

4 Tan, Z., Rohrer, F., Lu, K., Ma, X., Bohn, B., Broch, S., Dong, H., Fuchs, H., Gkatzelis,
5 G. I., Hofzumahaus, A., Holland, F., Li, X., Liu, Y., Liu, Y., Novelli, A., Shao, M., Wang,
6 H., Wu, Y., Zeng, L., Hu, M., Kiendler-Scharr, A., Wahner, A., and Zhang, Y.:
7 Wintertime photochemistry in Beijing: observations of RO_x radical concentrations in
8 the North China Plain during the BEST-ONE campaign, *Atmospheric Chemistry and*
9 *Physics*, 18, 12391–12411, <https://doi.org/10.5194/acp-18-12391-2018>, 2018.

10 Tan, Z., Lu, K., Jiang, M., Su, R., Wang, H., Lou, S., Fu, Q., Zhai, C., Tan, Q., Yue, D.,
11 Chen, D., Wang, Z., Xie, S., Zeng, L., and Zhang, Y.: Daytime atmospheric oxidation
12 capacity in four Chinese megacities during the photochemically polluted season: a case
13 study based on box model simulation, *Atmos. Chem. Phys.*, 19, 3493–3513,
14 <https://doi.org/10.5194/acp-19-3493-2019>, 2019.

15 Tan, Z., Ma, X., Lu, K., Jiang, M., Zou, Q., Wang, H., Zeng, L., and Zhang, Y.: Direct
16 evidence of local photochemical production driven ozone episode in Beijing: A case
17 study, *Science of The Total Environment*, 800, 148868,
18 <https://doi.org/10.1016/j.scitotenv.2021.148868>, 2021.

19 Wang, G., Iradukunda, Y., Shi, G., Sanga, P., Niu, X., and Wu, Z.: Hydroxyl,
20 hydroperoxyl free radicals determination methods in atmosphere and troposphere,
21 *Journal of Environmental Sciences*, 99, 324–335,
22 <https://doi.org/10.1016/j.jes.2020.06.038>, 2021.

23 Whalley, L. K., Stone, D., Dunmore, R., Hamilton, J., Hopkins, J. R., Lee, J. D., Lewis,
24 A. C., Williams, P., Kleffmann, J., Laufs, S., Woodward-Massey, R., and Heard, D. E.:
25 Understanding in situ ozone production in the summertime through radical observations
26 and modelling studies during the Clean air for London project (ClearfLo), *Atmos. Chem.*
27 *Phys.*, 18, 2547–2571, <https://doi.org/10.5194/acp-18-2547-2018>, 2018.

1 Whalley, L. K., Slater, E. J., Woodward-Massey, R., Ye, C., Lee, J. D., Squires, F.,
2 Hopkins, J. R., Dunmore, R. E., Shaw, M., Hamilton, J. F., Lewis, A. C., Mehra, A.,
3 Worrall, S. D., Bacak, A., Bannan, T. J., Coe, H., Percival, C. J., Ouyang, B., Jones, R.
4 L., Crilley, L. R., Kramer, L. J., Bloss, W. J., Vu, T., Kotthaus, S., Grimmond, S., Sun,
5 Y., Xu, W., Yue, S., Ren, L., Acton, W. J. F., Hewitt, C. N., Wang, X., Fu, P., and Heard,
6 D. E.: Evaluating the sensitivity of radical chemistry and ozone formation to ambient
7 VOCs and NO_x in Beijing, *Atmospheric Chemistry and Physics*, 21, 2125–2147,
8 <https://doi.org/10.5194/acp-21-2125-2021>, 2021.

9 Woodward-Massey, R., Slater, E. J., Alen, J., Ingham, T., Cryer, D. R., Stimpson, L. M.,
10 Ye, C., Seakins, P. W., Whalley, L. K., and Heard, D. E.: Implementation of a chemical
11 background method for atmospheric OH measurements by laser-induced fluorescence:
12 characterisation and observations from the UK and China, *Atmospheric Measurement
Techniques*, 13, 3119–3146, <https://doi.org/10.5194/amt-13-3119-2020>, 2020.

14 Yang, X.: A Review of the Direct Measurement of Total OH Reactivity: Ambient Air
15 and Vehicular Emission, *Sustainability*, 15, 16246,
16 <https://doi.org/10.3390/su152316246>, 2023.

17 Yao, Z., Shen, X., Ye, Y., Cao, X., Jiang, X., Zhang, Y., and He, K.: On-road emission
18 characteristics of VOCs from diesel trucks in Beijing, China, *Atmos. Environ.*, 103, 87–
19 93, <https://doi.org/10.1016/j.atmosenv.2014.12.028>, 2015.

20 Zhang, G., Hu, R., Xie, P., Lu, K., Lou, S., Liu, X., Li, X., Wang, F., Wang, Y., Yang,
21 X., Cai, H., Wang, Y., and Liu, W.: Intercomparison of OH radical measurement in a
22 complex atmosphere in Chengdu, China, *Science of The Total Environment*, 838,
23 155924, <https://doi.org/10.1016/j.scitotenv.2022.155924>, 2022a.

24 Zhang, G., Hu, R., Xie, P., Lou, S., Wang, F., Wang, Y., Qin, M., Li, X., Liu, X., Wang,
25 Y., and Liu, W.: Observation and simulation of HO_x radicals in an urban area in
26 Shanghai, China, *Science of The Total Environment*, 810, 152275,
27 <https://doi.org/10.1016/j.scitotenv.2021.152275>, 2022b.

1 Zou, Z., Chen, Q., Xia, M., Yuan, Q., Chen, Y., Wang, Y., Xiong, E., Wang, Z., and
2 Wang, T.: OH measurements in the coastal atmosphere of South China: possible
3 missing OH sinks in aged air masses, *Atmospheric Chemistry and Physics*, 23, 7057–
4 7074, <https://doi.org/10.5194/acp-23-7057-2023>, 2023.

5